

Direct Numerical Simulation of Cellular Structures in Jet Diffusion Flames

A dissertation submitted to
ETH Zurich

for the degree of
Doctor of Sciences

presented by
Adrian Luzi Valär
Dipl. Masch.-Ing. ETH

born 25 May 1975
citizen of Zuoz and Davos, GR

accepted on the recommendation of

Prof. Dr. K. Boulouchos, examiner

Prof. Dr. P. Papas, co-examiner

Dr. C. E. Frouzakis, co-examiner

Abstract

Three-dimensional, direct numerical simulations of cellular jet flames were performed to elucidate the nature of cellular structures in jet diffusion flames close to extinction. Such cellular structures were reported for flames near the extinction limit if the reactant Lewis numbers are below unity. The first part of this work consisted of extending an existing direct numerical simulation code for low Mach number reactive flows. Detailed, multi-step chemical description and detailed evaluation of the transport properties was added by coupling the code with the Chemkin libraries and a new scalable solver for the fully implicit integration of the stiff system of energy and species conservation equations. The extended numerical code was validated against numerical opposed-jet results and applied to the experimental investigation of an opposed-jet diffusion/edge flame. The detailed results obtained by direct numerical simulation enhanced the understanding of the experimentally observed phenomenon of a hysteretic by-stability of the diffusion and edge flames.

The simulation of cellular structures in jet diffusion flames was based on a recent experimental investigation of the formation of different cellular structures in weakly burning flames with varied jet and co-flow compositions and velocities. The fuel and oxidizer were hydrogen and oxygen, respectively, both diluted with carbon dioxide. Despite many difficulties inherent with the simulation of weakly burning flames, the experimental findings could be reproduced numerically. The analysis of the cellular structures gave insight to the involved physical processes associated with the formation of the cellular flames in a non-premixed jet configuration. An additional investigation on the dependency of the resulting cellular structure of the jet diffusion flame on the initial velocity profile of the jet enhanced the general understanding of the investigated phenomenon. Furthermore, it revealed the proportional dependency of the number of cellular structures on the initial vorticity thickness of the jet.

Zusammenfassung

Im Rahmen dieser Arbeit wurden zellulare Jet Flammen und ihre Entstehung untersucht. Dabei wurden dreidimensionale, direkte numerische Simulationen von Jetdiffusionsflammen nahe der Auslöschung durchgeführt mit dem Ziel, die bei der Bildung der zellularen Flammstabilitäten beteiligten Mechanismen zu verstehen. Auf die Entstehung von zellularen Flammstabilitäten wurde bereits in verschiedenen Publikationen zu Diffusionsflammen mit tiefen Lewis Zahlen und tiefer Verbrennungsintensität hingewiesen.

Im ersten Teil dieser Arbeit wurde, auf der Basis eines bestehenden Codes, ein dreidimensionaler, direkter numerischer Code für die Berechnung von reaktiven Strömungen mit detaillierter Evaluation der chemischen Quellterme und der einzelnen Transporteigenschaften entwickelt. Der erweiterte Code wurde erfolgreich mit existierenden numerischen und experimentellen Resultaten von Flammen in einem Gegenstrombrenner validiert. Zudem konnte anhand der Auswertungen die physikalische Grundlage der berechneten Diffusions- und "Edge"-Flammen sowie ihrer transienten Umformung untersucht werden.

Der Simulation von zellularen Strukturen in Diffusionsflammen lag eine kürzlich präsentierte experimentelle Untersuchung zu Grunde. Darin wurde die Bildung unterschiedlicher Strukturen in einer Freistrahldiffusionsflamme in Abhängigkeit der Strahlgeschwindigkeit und Gaszusammensetzung untersucht. Basierend auf diesen Experimenten konnten durch die in dieser Arbeit durchgeführten Simulationen neue Erkenntnisse über die Struktur und die Entstehung von zellularen Diffusionsflammen erlangt werden.

Eine Analyse der Abhängigkeit der Flammstruktur vom Strömungsprofil des Brennstoffstrahls zeigte, dass sich die Zahl der Strukturen in der Flamme proportional zu der Steilheit des angesetzten Strömungsprofils verhält.

Contents

Abstract	i
Zusammenfassung	i
Contents	iv
1 Introduction	1
1.1 Combustion and its numerical simulation	2
1.2 Jet diffusion flames	3
1.3 Combustion instabilities	5
1.3.1 Cellular flames	7
2 Spectral Element Code	13
2.1 Conservation equations	13
2.1.1 Continuum approximation and Navier-Stokes equations	14
2.1.2 Diffusion	17
2.1.3 Evaluation of the reaction rates	19
2.2 Spatial discretization	20
2.2.1 Spectral discretization techniques	21
2.2.2 Spectral element code	22
2.3 Temporal discretization	23
2.3.1 Splitting approach	23
2.3.2 Thermochemistry subsystem	24
2.4 Code validation	25
2.4.1 Computational set up and results	25
2.5 Summary	26

3	Opposed-jet diffusion flame instabilities	29
3.1	Opposed-jet flames	29
3.2	Experimental set-up	31
3.3	Simulation results	33
3.4	Conclusions	45
4	Cellular jet flames	49
4.1	Experimental set-up and measurement techniques	49
4.1.1	Experimental Results	52
4.2	Computational set-up	57
4.3	Comparison with the experiments	61
4.3.1	Case A: Variation of jet and co-flow composition	61
4.3.2	Case B: Variation of the jet composition and velocity	63
4.3.3	Variation of the jet velocity profile	81
4.3.4	Rotating cellular flame	83
4.4	Conclusions	88
5	Conclusions and Outlook	91
5.1	Thesis summary	91
5.2	Future work	93
	Bibliography	94
	Appendix	99
A	CVODE	101
B	Curriculum Vitae	105
	Curriculum Vitae	104

Chapter 1

Introduction

Combustion and its control are cornerstones in the development of mankind and is a basis of the cultural evolution. From what is known today, the first fire that was exploited and controlled by humans, was burning 790'000 years ago in the region of today's Israel [25]. About 500'000 years ago the first fire place was established in Europe and since then fire has played an increasing role until the beginning of the 18th century when combustion was used for the first time to generate mechanical work by a steam-engine. This development gave rise to the uncoupling of the demand of mechanical energy from the muscularity and is the reason for the fast technical progression in the last 300 years. Combustion is by far the most applied energy conversion technique nowadays and today's life is unthinkable without it. The process of combustion is very complex and multi-faceted and generations of scientists have dedicated their professional life to the understanding of the processes involved. Nevertheless, combustion, which is applied and benefitted by man since three-quarters of a million years, is not yet fully understood and its complexity suggests, that this will not change in the near future. This lack in knowledge is one of the reasons, why combustion is so fascinating and also the reason why this work is presented here.

1.1 Combustion and its numerical simulation

Combustion is a very difficult engineering problem, because of the strong coupling of fluid dynamics, thermodynamics and chemistry. These three fields have to be understood in order to analyze combustion processes.

A first and with respect to the complexity of the problem very important differentiation of combustion processes, is the physical state of the fuel and oxidizer. While the oxidizer is most often gaseous oxygen, most practical applications deal with solid or liquid fuel. Combustion problems which include evaporation or pyrolysis of the fuel are physically very complex and detailed numerical simulations of these problems are not yet possible. Often the complexity and non-uniformity of the generated gaseous fuel bears an additional demanding challenge to the problem. Simple combustion applications like a candle are numerically of the most demanding.

As mentioned above, one important aspect of combustion processes is the fluid-dynamic part. The flow, in which combustion takes place is important for the mixture, the stabilization of the flame and the transport of heat and combustion products. In most of the industrial applications, the flow is turbulent. The interaction of the combustion process with the flow is crucial in turbulent combustion and therefore an accurate simulation of the flow is very important. In most industrial applications an accurate simulation of the turbulent flow field is very expensive in terms of computational time, turbulent models are used to model the small scale eddies of the turbulent flow field. These simulations solve either the Reynolds averaged Navier Stokes (RANS) equations and use a turbulence model for the fluctuating part of the velocity components, or LES (Large Eddy Simulation), where only the smallest eddies are modelled, while most of the flow is simulated accurately. For combustion simulations, the turbulence models must be coupled to combustion models, which take the transport of heat and species due to the modelled turbulent flow as well as fluctuations of species and temperature beyond the simulated scales into account. In DNS (direct numerical simulations) no models are applied neither for the simulation of the turbulent flow field, nor for the combustion processes. The simulation of combustion processes without models requires resolution of all time and length scales, including the smallest turbulent structures and the flame structure. These requirement make DNS of real industrial applications computationally intractable. DNS simulations are often either of scientific interest or they are used for the development or the validation of turbulent and combustion models.

The numerical code presented in this work is a three-dimensional DNS code with detailed chemistry and detailed transport properties and is presented in detail in chapter 2.

1.2 Jet diffusion flames

Jet flames are very important in industrial applications and can be observed in many devices ranging from a simple lighter to large, megawatt burners in gas turbines. In most of these applications, non-premixed jet combustion takes place, mainly due to the simplicity of the concept. According to the associated flow conditions, laminar and turbulent jet flames can be distinguished. Within the scope of this work, only laminar non-premixed flames are investigated. In non-premixed flames, fuel and oxidizer are initially separated and must be brought together prior to combustion. In laminar jet flames, mixing is accomplished by molecular diffusion whose time scale is generally longer than those associated with chemical reactions. Hence, these systems are diffusion limited and are often called diffusion flames.

A simple theoretical description of diffusion flames in the limit of infinitely fast chemical reactions is known as the Burke-Schumann approximation [4], where the diffusion flame can be treated as a flame sheet. The concentration of both reactants become zero in the flame zone and the rates of diffusive transport of fuel and oxidizer to the reaction zone are in stoichiometric proportions. The most commonly considered configuration of a Burke-Schumann flame is a cylindrical tube from which fuel emerges into a concentric duct through which oxidizer is flowing with the same velocity as the fuel. Since the flame will always be positioned according to the stoichiometric proportions, the concentrations in the two flows define the position of the flame as long as preferential diffusion effects can be ignored. Therefore the position of the flame is depending on the initial mixture strength (ϕ), which is an important parameter in the analysis of non-premixed flames and is defined as the ratio of the initial fuel to the oxidizer concentrations in their respective streams normalized by the corresponding stoichiometric ratio. As it is indicated in figure 1.1, an under-ventilated flame, where the ϕ is larger than unity bends towards the walls of the duct, while a over-ventilated flame forms a tip on the symmetry axis of the tube. Y_O , Y_F and v are the mass fraction of oxidizer in the co-flow, the mass fraction of fuel in the jet and the jet and co-flow velocity, respectively.

However, the flame location does not depend only on the initial

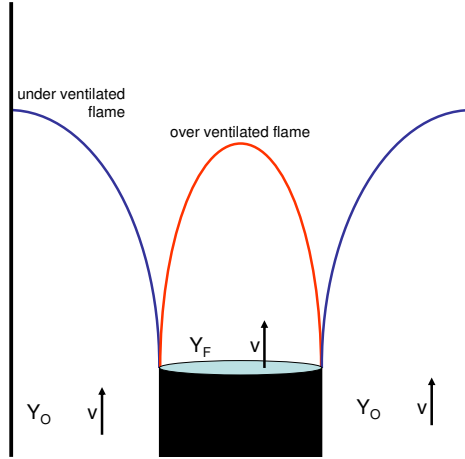


Figure 1.1: Schematic of a jet-diffusion flame with the locations of the flame for over- (red) and under-ventilated (blue) flames.

mixture strength, but also on the ratio of reactant fluxes towards the flame and heat fluxes away from the flame zone. A detailed description of this flame model is given by Williams [54]. In real flames, different diffusion coefficients and heat conductivities in the fuel and oxidizer stream influence the shape of the flame as well.

The ratio of the characteristic diffusion time to the chemical time is defined as the Damköhler number ($Da = \tau_{diff}/\tau_{chem}$). The Burke-Schumann approximation holds for chemical reactions which are very fast compared to the characteristic diffusion time, corresponding to large Da . For moderate values of Da , combustion is incomplete and there is leakage of one or both reactants through the reaction zone. The importance of the mixing rate or the characteristic diffusion time in the investigation of diffusion flames brings a strong coupling of the flame to its aerodynamic conditions. The first theoretical investigation on the structure of steady counterflow diffusion flames was presented by Liñán [37] who considered a flame with a single-step reaction with large activation energy. The results are summarized in a plot of the maximum flame temperature against Da resulting in the S-shaped curve presented in figure 1.2, where T_c , $T_{F,0}$, $T_{O,0}$, Da_E and Da_I are the combustion temperature, the initial fuel and oxidizer temperature, the extinction Da and the ignition Da , respectively.

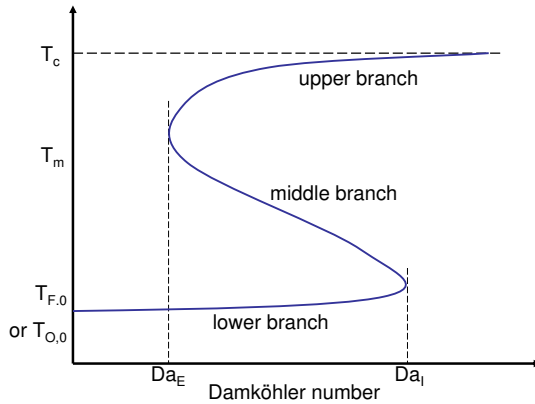


Figure 1.2: Qualitative relation of the reaction-temperature of a diffusion flame to the Damköhler number [37].

Figure 1.2 consists of three branches, from which the lower branch corresponds to a nearly-frozen or slow-reaction regime, where the temperature increase due to chemical reactions is very small. The middle branch is unstable and represents a regime where the reactants leak through the reaction zone. The upper branch represents the intensely burning flame, where for high Da , the flame is only diffusion controlled and is close to the earlier discussed Burke-Schumann flame. The cellular diffusion flames, which are the main focus of this work are in the region of lower Da , where diffusive and chemical timescales are similar. The Da of these flames is close to the extinction limit (Da_E).

1.3 Combustion instabilities

Many different types of combustion instabilities have been observed. Some of them are intrinsic flame instabilities, where the source of the instability is the flame itself. Instabilities in large engineering devices like gas turbines or rocket motors are often not only influenced by the flame itself, but also by a large number of parameters, like size and shape of the combustion chamber, the fuel, the air-fuel ratio and so on. They are important

problems in industrial applications and are often coupled to acoustic instabilities.

Three different effects can result in intrinsic flame instabilities: flow field effects, thermo-diffusive effects and buoyancy effects. The investigation of these intrinsic instabilities is usually done in experiments, that try to decouple the different instability mechanisms.

The most important hydrodynamic instability in a jet is the Kelvin-Helmholtz instability, which emerges in the shear layer of the jet. This instability, which was first investigated by Kelvin in the second half of the 19th century, is not triggered by the flame even though it might be strongly influenced by it [49]. Flow field driven flame instabilities arise due to the influence of the flame on the flow. The gas expansion during combustion may accelerate the flow and, depending on the configuration, lead to flame instabilities [54].

Two different combustion-driven instabilities associated with thermal-diffusive effects have been observed, depending on the species Lewis numbers and the thermal diffusivity. Therefore these instabilities evolve due to the difference of energy and species diffusive fluxes. The Lewis number is a dimensionless number defined as the ratio of the thermal diffusivity to the mass diffusivity of one species into the mixture ($Le_i = \lambda / \rho c_p D_i$, where λ is the heat conductivity of the gas, ρ the density, c_p the specific heat and D_i the diffusivity of species i , respectively).

The two types of thermo-diffusive instabilities can be distinguished as follows: If the species diffusion of the reaction limiting species is faster, than the thermal diffusion ($Le < 1$), cellular flames may develop. If the thermal diffusion is faster than the one of the species ($Le > 1$), pulsation in the flame may arise. Matalon [41] showed, that this pulsation arise due to a deficiency in enthalpy in the reaction zone if the Lewis numbers of fuel and oxidizer are sufficiently large.

Buoyancy driven instabilities are triggered by the density difference in the flame and its influence due to the gravitational field. A flame front or a flame sheet in a diffusion flame is associated with a large change in density, which is responsible for these instabilities. The change in density is mainly due to the temperature dependency of the density, which would be strictly proportional to the inverse of temperature for a perfect gas. These instabilities are commonly seen in vertical upwards propagating flame fronts in premixed flames, where burned, light gas is below the unburned, heavy gas. Such a configuration leads to Rayleigh-Taylor instabilities [54].

In this work, the focus is on cellular instabilities in jet diffusion flames. The next section gives an extensive description of the problem and the

investigations done so far.

1.3.1 Cellular flames

The formation of cellular structures in flames due to thermo-diffusive effects was observed and documented a long time ago. The systematic investigation of this phenomenon covers mainly cellular instabilities in premixed flames, where elaborate experimental as well as analytical and numerical work has been performed. Clavin [12], Bychkov and Liberman [5] and Matalon [41] give extended reviews on instabilities in premixed flames.

Intrinsic instabilities have not been studied as extensively in diffusion flames as in premixed configurations. In the case of the cellular flames, the involved mechanisms during the formation of the cellular structures are very similar, but their behavior, shape and size might be influenced by their completely different environment. The triggering mechanism in the formation of cellular structures in a jet diffusion flames are discussed below.

Figure 1.3 shows a schematic of a simplified jet diffusion flame. The center circle indicated the nozzle dimensions of the fuel jet which is surrounded by the oxidizer co-flow. An unperturbed strongly burning flame would build a perfectly round circle. The red line indicates the location of the flame which is perturbed. This perturbation might have any cause and is a prerequisite for the formation of cellular structures. Due to the perturbation the flame acquires convex and concave regions towards the fuel and the oxidizer side. While a convex region increases the surface, a concave one decreases the surface compared to the perfectly round flame. In a convex region, the surface is increased and so does the species flow towards the flame, while heat diffusion away from the flame increases simultaneously. A convex structure can therefore be seen as a local source of one of the reactants and a local sink of heat. Depending on the relation of these two effects, the combustion intensity in the discussed structure of the flame either increases or decreases according to the Arrhenius relation (see section 2.1.3). For low reactant diffusion velocity and strong heat diffusion ($Le > 1$), the temperature in the convex part will decrease and accordingly, the combustion intensity will decrease. For a fast diffusing reactant in a gas mixtures with low heat diffusivity ($Le < 1$), the reaction intensity will increase. In a diffusion flame, where such convex structures can form either towards the oxidizer or the fuel side, the influence of the reaction limiting reactant, which is completely consumed during combustion, has a much stronger effect on the combustion intensity.

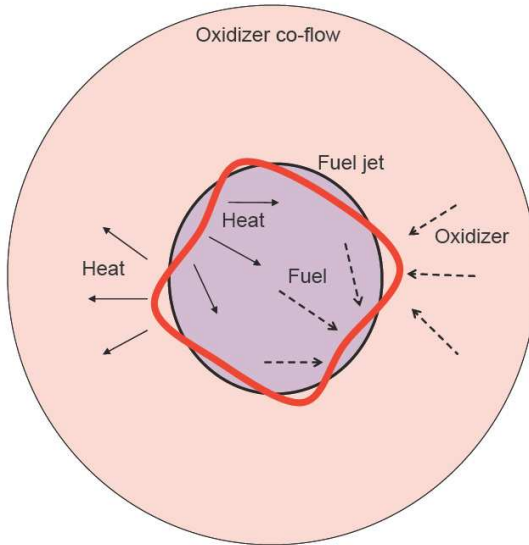


Figure 1.3: Schematic of a diffusion jet flame (including oxidizer co-flow) in the top view with infinitely fast reaction assumed. The flame is perturbed and differs from the perfectly round shape (red). The diffusion of species (dashed) and energy (solid) is indicated with arrows.

The first cellular structure in diffusion flames were reported by Garside et al. in 1951 [23], in a N_2 - or CO_2 -diluted hydrogen-air jet flame. The observed five cell structure in a jet diffusion flame with carbon dioxide diluted hydrogen (19.35 mole% H_2) could be shown to rotate or remain stationary by adjusting the flow rate. Two years later, a detailed parametric study including the effects of pressure, flow rate and different fuels was published [24]. The influence of the differences in diffusion velocity was recognized and the formation of the cellular structure linked to the availability of fast diffusing hydrogen or deuterium.

Dongworth et al. [15] 25 years later reported cellular patterns in a hydrogen-oxygen splitter-plate burner for N_2 diluted reactants. By analyzing the response of the flame to acoustic disturbances, acoustic effects could be eliminated as source of cellular flames. Further investigations included the variation of the inert gas in the fuel as well as in the oxidizer

stream. It could be shown that, for the applied lean mixtures, an increase of the mole weight of the inert gas (from N_2 to Ar) favors the formation of the cellular structures, while its reduction (from N_2 to He) leads to disappearance of the cells.

Ishizuka et al. [28] investigate the concentration limits of diffusion flames in a counterflow diffusion flame established in the forward stagnation region of a porous cylinder. Methane or hydrogen were diluted with nitrogen, argon or helium in order to analyze the effects of non-uniform transport properties on the flame temperature. The fuel was fed through the porous cylinder into the uniform stream of diluted oxygen. The uniform flame front of a hydrogen flame, diluted with excess nitrogen or argon, transformed into a striped-pattern flame. It could also be shown, that the flame temperature increases for a fuel Lewis number below unity.

From the fact that this phenomenon could not be seen for helium-diluted flames, Ishizuka et al. linked this diffusion flame phenomenon to the cellular flames observed in premixed hydrogen-oxygen flames. Since cellular patterns could only be stabilized for lean mixtures, the essential role of the preferential diffusion of hydrogen in the occurrence of these striped-pattern flames could be shown.

Together with the findings of Zhang et al. [56], who linked the cellular structures observed in a flame spreading over thin solid fuel to Lewis number (Le) effects, Chen et al. [8] demonstrated that for the formation of cellular flames, two conditions have to be fulfilled independently: The flame has to be close to extinction and Le of the reaction limiting component has to be sufficiently smaller than unity. A parametric study, where the Lewis number of the fuel (Le_F) and oxidizer (Le_O) were varied in a slot burner flame, was performed. The Le variation was done using H_2 , CH_4 and C_3H_8 as fuel and different inert diluter (He , N_2 , Ar , CO_2 and SF_6). In order to substantiate the obtained results, Chen et al. reanalyzed all the previous results showing cellular patterns in diffusion flames [23, 15, 28, 56] and could show that all the reported cellular flames satisfied the two conditions.

The experimental findings of Chen et al. [8] were verified by the analytical work of Kim et al. [32, 31], where a stability analysis of a counterflow diffusion flame configuration was carried out. Kim et al. also mention the problem of investigating cellular diffusion flames in a jet configuration due to the lifted flame and the partially premixing associated with it. Therefore, the variations of the jet lift-off height might adulterate the one to one analysis of cause and effect in the flame.

Füri [22] investigated diffusion jet flame instabilities experimentally in

a laminar jet configuration. The vertical fuel jet was surrounded by an oxidizer co-flow emerging from a porous plate. By varying the jet and co-flow velocities and composition, thermo-diffusive instabilities as well as Kelvin-Helmholtz instabilities were investigated. The investigations of the thermo-diffusive instabilities included cellular flames as well as pulsating flames and both were investigated concerning the instability onset limits of fuel and oxidizer Lewis numbers. In a SF_6 -diluted methane jet flames with a diluted oxygen co-flow, depending on the ratio of jet and co-flow velocity, either stationary or rotating cells were reported. The experimental onset limits for the Lewis numbers could successfully be matched to the analytical results of Cheatham et al. [7]. This result couples the critical Lewis numbers of fuel and oxidizer for the formation of the cellular structures, and shows that the concept of the one “effective” single Lewis number concept, successfully applied to premixed flames, is not sufficient for diffusion flame instabilities.

Papas et al. [44] demonstrated by linear stability analysis of a simplified diffusion flame model allowing for hydrodynamic effects, that similar mechanisms are active for jet diffusion flames as for the earlier reported opposed-jet flames. A more extended analytical investigation on the same problem was reported by Rais [49] including a detailed parametric study of Le , jet and co-flow velocities and stoichiometry. For relatively high Le near or greater than unity, an axisymmetric mode was shown to be dominant. While for relatively low Le of fuel and oxidizer, near the extinction limit the cellular modes have been shown to be dominant. The development of cellular instabilities in flames with fuel Le equal or below unity, could be shown to be dependent of oxidizer Le as well as initial mixture strength. According to earlier investigations [7], the propensity for cellular instabilities could be shown to increase with decreasing initial mixture strength.

The first experimental work concentrating on the systematical investigation of the cellular structures in jet diffusion flames was performed by Lo Jacono [40, 38, 39]. This parametric study was performed in an axisymmetric jet burner with a uniform oxidizer co-flow. For the jet flames close to extinction, the influence of the jet and co-flow composition were reported for a CO_2 -diluted hydrogen, oxygen flame. Different numbers of cells in the azimuthal direction, associated with different wave numbers, were observed and referred to as different cellular modes. For a given initial mixture strength, several cellular states were found to co-exist near the extinction limit and the preferred number of cells was observed to decrease with decreasing oxygen concentration.

Later on a different parametric study by Lo Jacono [38] reports the regions of stable combustion, cellular instabilities and extinction for the fuel concentration in an axisymmetric, CO_2 -diluted hydrogen jet with a constant velocity, constant composition co-flow. This investigation was performed for a large range of jet velocities and varying fuel compositions. In the region of cellular instabilities, the different cellular modes were reported including their hysteretic behavior. A correlation of the inlet velocity profile of the jet with the cellular mode was found. This experimental work is the basis for the numerical investigations presented in this thesis. In chapter 4 the comparison of the findings reported by Lo Jacono and the simulation results obtained from the simulations accomplished during this work is given.

A recent stability analysis of a planar diffusion flame by Metzener and Matalon [42] reports the formation of cellular patterns for Le lower than unity and fuel-lean conditions. Since in a planar flame, the influence of the flow field on the cells is not as strong as in jet diffusion flames, the cells showed characteristic dimensions corresponding to the diffusion length or the reaction zone dimension as it was observed in cellular premixed flames. Metzener and Matalon investigated the influences of a range of physical parameters as Le of fuel and oxidizer, initial mixture fraction and flow conditions. For $Le > 1$ and fuel-rich conditions, pulsation instabilities were observed and oscillating cellular structures were documented, in regions of competing modes of instability.

First three-dimensional simulations of cellular flame instabilities of CO_2 -diluted H_2 jet diffusion flames close to extinction were performed with single-step chemistry and constant but unequal reactant Le by Frouzakis et al. [21]. The experimental observations of [40] were reproduced numerically by three-dimensional DNS and linear stability analysis. The co-existence of different cellular modes as well as the increasing propensity for cellular instabilities with decreasing reactant Le and Da , could be reproduced numerically, albeit only qualitatively.

In this work, three-dimensional DNS with detailed chemistry and transport were performed with the aim of reproducing the experimental findings of [40, 38] quantitatively. The numerical investigation provides detailed, quantitative results on the cellular flames and its transition from one mode to another. This information is evaluated and discussed in order to enhance the understanding of the phenomenon. The work had two main parts: First, an existing, three-dimensional spectral element DNS code was extended by including detailed chemistry and detailed transport properties. Associated with this extension of the code, was a change of the

numerical scheme for the temporal integration of the thermo-chemistry part to a scheme accounting for the additional stiffness in the system. The enhanced code was validated against numerical as well as experimental results of opposed jet diffusion flames. Then the code was applied to the study of cellular instabilities in jet diffusion flames. The formation limits as well as the inter cellular structure of the flame were investigated and the results were analyzed and compared to the available experimental results.

The thesis is structured as follows: In chapter 2 the code which is developed and applied in this work is presented. The governing equations and a detailed discussion of the diffusion and chemical terms are discussed and the spatial and temporal discretization are presented. The first validation steps against numerically obtained opposed-jet results is shown. In chapter 3, opposed-jet flame simulations are presented, which reproduce experimental investigations performed by Ciani [10, 11]. The comparison of the numerical results to the experimental findings is given and transient investigations of the opposed-jet flame changing from a diffusion to a ring shaped edge flame are presented. In chapter 4 cellular jet flame results are presented, together with the experimental set-up used by Lo Jacono [40, 38]. Also the computational set-up of the performed simulations including the computational domain and the applied boundary conditions are presented. The numerical results are compared to the experimental findings and the detailed temperature and species fields were analyzed. Different dependencies of the cellular configuration on the applied boundary conditions were investigated. In chapter 5 the main conclusions of this work are given.

Chapter 2

Spectral Element Code

The numerical simulations in this work were performed using a low Mach number spectral element code. This code, written in Fortran and C, is originally based on a incompressible, parallel three dimensional code [17]. During previous works, the code was extended for the simulation of low Mach number, non-isothermal, multi species flows with single-step chemistry. The further extension of the code was a major part of the presented work and a necessity for the application of the code to the problem of interest. During this work, detailed chemistry and transport properties were integrated in the existing code. This extensions have all been done under the consideration of the parallel architecture of the original code. In this chapter, the governing equations are presented first (section 2.1). The calculation of the chemical source terms with the Chemkin library is explained in section 2.1.3. The temporal discretization (see 2.3) for the simulation of combustion problems is strongly influenced by the large range of time-scales involved, which lead to a stiff system and the associate restrictions in the choice of the temporal integration scheme. The spatial discretization is presented in section 2.2. An overview of the temporal discretization is given in section 2.3. In section 2.4 the validation of the code against numerical opposed-jet results is presented. At the end of the chapter, the chapter is summarized (section 2.5).

2.1 Conservation equations

In this section, the physical model is presented. This model is the low Mach number formulation of the Navier-Stokes equation which is pre-

sented in section 2.1.1. The diffusion term of this equation is presented in detail in section 2.1.2 and the evaluation of the reaction terms and transport properties is presented in section 2.1.3.

The discretization of the here presented physical model in space and time is presented in the following sections 2.2 and 2.3.

2.1.1 Continuum approximation and Navier-Stokes equations

Gaseous substances consist of a huge number of molecules (1 cm^3 gas at $0^\circ C$ and 1 atm consists of $2.69 \cdot 10^{19}$ molecules) and for the simulation of the motion of these molecules, the appropriate laws of motion would have to be applied to each of them. Since such simulations would exceed nowadays computational possibilities, the continuum approximation, which states, that a fluid is a continuous substance, is employed instead. Wilcox [53] gives a distinct summary of the conditions which have to be fulfilled in order to justify this approximation. It is a statistical approximation and therefore, the volume in which a sufficient number of particles is present, in order to find meaningful statistical averages, has to be small compared to the geometrical dimensions of the problem. As a result of the continuum approximation and the assumption that the fields of interest (velocity, pressure, density and temperature) are differentiable, what excludes phase transition and two phase flows, lead to the Navier-Stokes Equations, which are derived from the leading principles of the conservation of mass, momentum and energy.

The spectral element code solves the Navier-Stokes equations together with the energy and species equations in the low-Mach number limit, i.e. free of acoustic wave interactions [9]. The low-Mach number formulation is derived by expansion of the variables in power series of the Mach number as illustrated for the pressure in equation (2.1).

$$p = p_0 + Ma \cdot p_1 + Ma^2 \cdot p_2 + O(Ma^3), \quad (2.1)$$

where p_0, p_1 and p_2 are the leading, first- and second- order pressure, respectively.

At the limit of the Mach number approaching zero, the pressure remains at leading order in the energy and state equations and at first order in the momentum equation. The equations are formulated for an open system, where the leading term is the thermodynamic pressure which is not only constant in space but also in time. The resulting equations are the continuity equation:

$$\frac{\partial \rho}{\partial t} + \nabla \cdot (\rho \underline{u}) = 0 \quad (2.2)$$

Equation (2.2) is the continuity equation, where ρ , t are density and time and \underline{u} is the velocity field; the momentum equations:

$$\rho \left[\frac{\partial \underline{u}}{\partial t} + \underline{u} \cdot \nabla \underline{u} \right] = -\nabla p_1 + \nabla \cdot (\mu \underline{\underline{S}}) + \rho \underline{\underline{g}}, \quad (2.3)$$

where

$$\underline{\underline{S}} = \nabla \underline{u} + (\nabla \underline{u})^T - \frac{2}{3}(\nabla \cdot \underline{u})\underline{\underline{I}} \quad (2.4)$$

Equation (2.3) is the momentum conservation equation, where μ , $\underline{\underline{S}}$, $\underline{\underline{I}}$ and $\underline{\underline{g}}$ are dynamic viscosity, shear stress tensor, unit tensor and gravitational acceleration vector, respectively; the energy conservation equation:

$$\begin{aligned} \rho c_p^a \left[\frac{\partial T}{\partial t} + \underline{u} \cdot \nabla T \right] &= \nabla \cdot \lambda (\nabla T) + \sum_{i=1}^N h_i \dot{\omega}_i \\ &\quad - \nabla \cdot \rho T \sum_{i=1}^N c_{pi} Y_i \underline{V}_i + \frac{\partial p_0}{\partial t} \end{aligned} \quad (2.5)$$

$$c_p^a = \sum_{i=1}^N Y_i c_{pi}, \quad (2.6)$$

where T , c_{pi} , c_p^a , λ , h_i^0 , $\dot{\omega}_i$ and \underline{V}_i are temperature, species and mean heat capacity at constant pressure, thermal conductivity, total enthalpy, the chemical production term and the diffusion velocity of species i , respectively. It is simplified by neglecting the viscous forces energy term, since it is negligible in the cases of interest in this work. The body force term cancels out if no preferential forces exist. The last term on the right hand side, the temporal derivation of the thermodynamic pressure, is equal to zero for open systems, because the thermodynamic pressure is equal to the atmospheric pressure and therefore invariant in time.

Finally,

$$\rho \left[\frac{\partial Y_i}{\partial t} + \underline{u} \cdot \nabla Y_i \right] = -\nabla \cdot (\rho Y_i \underline{V}_i) + \dot{\omega}_i \quad i = 1, \dots, N, \quad (2.7)$$

are the species conservation equations, where Y_i is the mass fraction of species i and \underline{V}_i is the diffusion velocity of species i . The diffusion velocity is explained and discussed in detail in section 2.1.2.

An additional equation, the equation of state or ideal gas law

$$p_0 = \rho RT \quad (2.8)$$

is needed in order to close the system of low Mach number equations. This assumption is widely accepted for combustion problems at least as long as the pressure is low.

The numerical code solves the above presented equations in non-dimensionalized form. The variables and other symbols used and the corresponding reference quantities used for non-dimensionalization of the conservation equations are summarized in the following tables:

variables	symbol	reference values
velocity	\tilde{u}	\underline{u}_∞
length	\tilde{x}	L_∞
density	$\tilde{\rho}$	ρ_∞
chemical source term	$\tilde{\omega}_i$	$(L_\infty/u_\infty)/\rho_\infty$
diffusion coefficient	$\tilde{D}_{i,j}$	$D_{i,\infty}$
time	\tilde{t}	u_∞/L_∞
pressure	\tilde{p}	p_∞
dynamic viscosity	$\tilde{\mu}$	μ_∞
gravity	\tilde{g}	g_∞
temperature	\tilde{T}	T_∞
heat capacity	\tilde{c}_p^a	$c_{p,\infty}^a$
heat of formation	\tilde{h}_i^0	$c_{p,\infty}^a T_\infty$
heat conductivity	$\tilde{\lambda}$	λ_∞
diffusion velocity	\tilde{V}_i	\underline{u}_∞
mean molecular weight	\tilde{W}	W_∞
operators	symbol	reference values
divergence	$\tilde{\nabla} \cdot$	$1/L_\infty$
gradient	$\tilde{\nabla}$	$1/L_\infty$

Non-dimensional numbers are defined as

$$Re = \frac{u_\infty L_\infty \rho_\infty}{\mu_\infty} = \frac{u_\infty L_\infty}{\nu_\infty} \quad (2.9)$$

$$Sc_i = \frac{\mu_\infty}{\rho_\infty D_{i,\infty}} = \frac{\nu_\infty}{D_{i,\infty}} \quad (2.10)$$

$$Fr = \frac{u_\infty}{\sqrt{g L_\infty}} \quad (2.11)$$

$$Pr = \frac{c_{p\infty} \mu_\infty}{\lambda_\infty}, \quad (2.12)$$

where Re , Sc , Fr and Pr are Reynolds, Schmidt, Froude and Prandtl number, respectively.

The dimensionless equations are posted below

$$\frac{\partial \tilde{\rho}}{\partial \tilde{t}} + \tilde{\nabla} \cdot (\tilde{\rho} \tilde{\underline{u}}) = 0 \quad (2.13)$$

$$\tilde{\rho} \left[\frac{\partial \tilde{\underline{u}}}{\partial \tilde{t}} + (\tilde{\underline{u}} \cdot \tilde{\nabla}) \tilde{\underline{u}} \right] = -\tilde{\nabla} \tilde{p}_1 + \frac{1}{Re} \tilde{\nabla} \cdot (\tilde{\mu} \tilde{\underline{S}}) + \frac{1}{Fr^2} \tilde{\rho} \tilde{\underline{g}} \quad (2.14)$$

$$\begin{aligned} \tilde{\rho} \tilde{c}_p^a \left[\frac{\partial \tilde{T}}{\partial \tilde{t}} + \tilde{\underline{u}} \cdot \tilde{\nabla} \tilde{T} \right] &= \frac{1}{Re Pr} \tilde{\nabla} \cdot [\tilde{\lambda} (\tilde{\nabla} \tilde{T})] \\ &\quad - \sum_{i=1}^N \tilde{h}_i^0 \tilde{\omega}_i - \tilde{\nabla} \cdot \tilde{\rho} \tilde{T} \sum_{i=1}^N \tilde{c}_{pi} Y_i \tilde{\underline{V}}_i \end{aligned} \quad (2.15)$$

$$\tilde{\rho} \left[\frac{\partial Y_i}{\partial \tilde{t}} + \tilde{\underline{u}} \cdot \tilde{\nabla} Y_i \right] = -\frac{1}{Re Sc_i} [\tilde{\nabla} \cdot (\tilde{\rho} Y_i \tilde{\underline{V}}_i)] + \tilde{\omega}_i \quad (2.16)$$

$i = 1, \dots, N$

$$\tilde{\rho} = \frac{\tilde{W}}{\tilde{T}} \quad (2.17)$$

The tilde (\sim) assigning non dimensional quantities is omitted in the following discussion for simplicity, and only non dimensional quantities will be used from now on.

The system of equations (2.13) to (2.17) is solved by the numerical code which is used in this work. The evaluation of the diffusion term, which is the first term on the right hand side of equation (2.16), and the chemical source terms are discussed in more detail below.

2.1.2 Diffusion

The diffusion term appearing in the species-conservation equation is the most demanding and will be discussed here according to [14, 54].

The diffusion velocity (V_i) is the key variable in this term and can be calculated from the following equation, derived from the kinetic theory of gases:

$$\begin{aligned} \nabla X_i = & \sum_{j=1}^N \left(\frac{X_i X_j}{D_{ij}} \right) (\underline{V}_j - \underline{V}_i) + (Y_i - X_i) \left(\frac{\nabla p}{p} \right) + \left(\frac{\rho}{p} \right) \sum_{j=1}^N Y_i Y_j (f_i - f_j) \\ & + \sum_{j=1}^N \left[\left(\frac{X_i X_j}{\rho D_{ij}} \right) \left(\frac{D_{T,j}}{Y_j} - \frac{D_{T,i}}{Y_i} \right) \right] \left(\frac{\nabla T}{T} \right), \quad i = 1, \dots, N \end{aligned} \quad (2.18)$$

where X_i , Y_i , D_{ij} , f_i , $D_{T,i}$ are mole (volume) fractions, mass fractions, binary diffusion coefficients, body-force on species i and thermal diffusion coefficient of species i , respectively. For general combustion problems, the pressure variation is relatively small and the second term on the right-hand side can be neglected. The third term on the right hand side is only relevant for different external forces on the different species, which is the case for electro-magnetic forces on charged species, but is irrelevant for most combustion problems. The last term on the right-hand side of equation (2.18) is the so-called thermal diffusion. This term describes the tendency of light molecules to move to hot regions and heavy molecules to cold regions. This effect may be of importance for simulations including small molecules like hydrogen or small particles, which behave like large molecules and large temperature gradients, as can be observed if a flame touches a cold wall or a cold flow ignites at the hot wall. For the simulations presented here, this term is neglected despite the fact that hydrogen is used as fuel, because due to the relatively small temperature gradients, the term was found to be small [54]. For the simulation of the problems of interest, equation (2.18) reduces to the Stefan-Maxwell equation:

$$\nabla X_i = \sum_{j=1}^N \frac{X_i X_j}{D_{ij}} (\underline{V}_j - \underline{V}_i), \quad i = 1, \dots, N \quad (2.19)$$

The evaluation of the binary diffusion coefficient D_{ij} is computationally expensive and an effective diffusion coefficient D_i for each species i in the mixture is defined instead. This diffusion coefficient depends on the temperature, pressure and composition of the mixture and must be evaluated at every time step and every mesh point. With this simplification, the following Fick's-Law can be derived from equation (2.19):

$$Y_i \underline{V}_i = -D_i \nabla Y_i, \quad i = 1, \dots, N \quad (2.20)$$

These N equations, together with the requirement of mass conservation ($\sum_{i=1}^N Y_i = 1$) which appears as an additional equation, build an over determined system. Adding all the species equations (2.16) results in the equation of total mass conservation only if equation (2.21) and (2.22) are fulfilled. Due to the applied approximation of Fick's-Law, equation (2.21) is violated if not all the diffusion coefficient are equal ($D_i = D$).

$$\sum_{i=1}^N Y_i \underline{V}_i = 0 \quad (2.21)$$

$$\sum_{i=1}^N \dot{\omega} = 0 \quad (2.22)$$

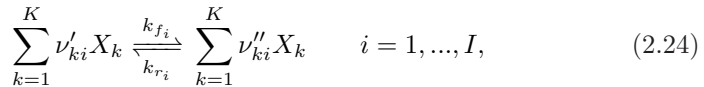
In order to enforce total mass conservation, the correction velocity (\underline{V}_c) can be introduced.

$$\underline{V}_i = \underline{V}_i^* + \underline{V}_c, \quad \text{where} \quad \underline{V}_c = - \sum_{i=1}^N Y_i \underline{V}_i^* \quad (2.23)$$

where \underline{V}_i^* is the result form Fick's law and \underline{V}_c is a correction velocity. \underline{V}_c varies in space, but is independent of the species. \underline{V}_i is applied to equation 2.16.

2.1.3 Evaluation of the reaction rates

The general form of the I elementary reactions involving K chemical species is



where ν_{ki} , X_k , k_{f_i} and k_{r_i} are the stoichiometric coefficients (integers), the chemical symbol for the k^{th} species and the forward and reverse rate constants of the i^{th} reaction, respectively. The production rate of the k^{th} species ($\dot{\omega}_k$) can be written as a summation of the rate of all reactions involving the k^{th} species [30].

$$\dot{\omega}_k = \sum_{i=1}^I (\nu''_{ki} - \nu'_{ki}) q_i \quad k = 1, \dots, K, \quad (2.25)$$

where q_i is the rate of the i^{th} reaction given by the difference of the forward and the reverse rates

$$q_i = k_{f_i} \prod_{k=1}^K [X_k]^{\nu'_{ki}} - k_{r_i} \prod_{k=1}^K [X_k]^{\nu''_{ki}} \quad (2.26)$$

where $[X_k]$ is the molar concentration of the k^{th} species. The forward rate constants of the i^{th} reaction are given by the extended Arrhenius expression

$$k_{f_i} = A_i T^{\beta_i} \cdot e^{-E_i/RT}, \quad (2.27)$$

where A_i is the pre-exponential factor and β_i , R , E_i and T are temperature exponent, the ideal gas constant, the activation energy and the temperature, respectively. For a reaction, the term $e^{-E/RT}$ represents the fraction of the molecules, which have enough energy to overcome the activation energy barrier. The factor A_i includes other influences as collision frequencies and the spatial orientation of the molecules relative to each other [43].

The implementation of detailed chemistry source terms have large influence on the numerical behavior of the system of equations. The coupling of fast and slow reactions with the flow field, increase the numerical stiffness of the system of equations. The subject of stiffness and its treatment are discussed in [33].

For the detailed evaluation of the chemical source terms, the code was coupled to the CHEMKIN-II [30] package. Mixture-average transport is used for the evaluation of the transport properties, based on the CHEMKIN transport database [29].

2.2 Spatial discretization

The discretization of the spatial derivatives is done using the spectral element method, where the computational domain is divided into elements, within each of which, the variables are represented by polynomial approximations approximated by high order polynomial. The spectral element approach combines the high-order accuracy of the spectral technique with the geometric flexibility of finite element methods to simulate complex geometries [17].

2.2.1 Spectral discretization techniques

Spectral schemes do not approximate the fields on a discrete mesh, but using continuous functions of degree N , in the form of equation (2.28)

$$\phi_A(x, t) = \sum_{k=0}^N a_k(t) \cdot \eta_k(x), \quad (2.28)$$

where ϕ_A , a_k and η_k are the approximated solution, the unknown coefficients which have to be computed and the trial functions, respectively. The derivation of the approximate solution (ϕ_A) requires the derivation of the trial functions. The derivation reduces the order of the trial function from N to $N - 1$ and the derivation of equation (2.28) can be written as in equation (2.29). N' and $a'_k(t)$ depend on N , $a_k(t)$ and on the choice of the trial function and are therefore known.

$$\frac{d}{dx} \phi_A(x, t) = \sum_{k=0}^{N'} a'_k(t) \cdot \eta_k(x) \quad (2.29)$$

The coefficients $a_k(t)$ can be computed from the residual $R(x, t)$ which, for a differential equation of the form $P(\phi, t) = 0$ is defined as $R(x, t) = P(\phi_A, t)$. This residual is weighted using a test function $\psi_k(\phi)$. In order to compute the coefficients $a_k(t)$, the integral over the domain G of the residual weighted with the $N + 1$ test functions is required to be zero.

$$\int_G \psi_k(x) \cdot R(x, t) dx = 0, \quad k = 0, \dots, N \quad (2.30)$$

The choice of the trial and test functions defines the type of the spectral method:

- The Galerkin method uses the same functions for test and trial functions ($\psi_k = \phi_k$).
- If the collocation method is applied, the residual is required to be zero at the collocation points x_0, \dots, x_N , therefore the test functions are defined as Dirac delta-functions ($\psi_j = \delta(x - x_k)$).
- The least squares method minimizes the value of the square of the residual integrated over the domain G .

As trial functions, usually, smooth, arbitrary differentiable functions, which are defined in the whole domain are chosen. Chebyshev or Legendre polynomials are the most commonly used.

2.2.2 Spectral element code

The code used in this work, is based on the spectral element method using Galerkin test functions and Legendre polynomial expansion through the Gauss-Lobatto-Legendre quadrature nodes, which are solutions to the equation

$$(1 - x^2)L'_N = 0, \quad x \in G, \quad (2.31)$$

where L'_N is the derivative of the Legendre polynomial of degree N . The associated Lagrangian interpolation functions are defined as

$$\pi_k(x) = \frac{-1}{N(N+1)} \frac{(1-x^2)L'_N(x)}{(x-x_k)L'_N(x_k)}, \quad 0 \leq k \leq N \quad (2.32)$$

In figure 2.1, the basis functions of the Lagrangian interpolation polynomial of degree $N = 6$ are plotted together with the corresponding solution of equation (2.31). The advantage of the combination of the Legendre polynomials with the Gauss-Lobatto-Legendre quadrature nodes is that

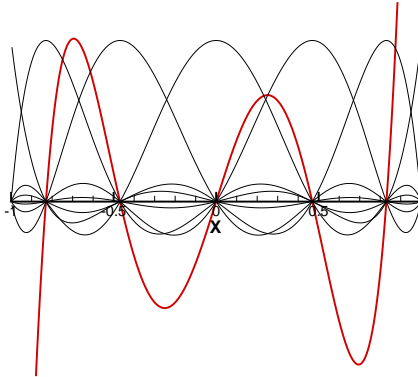


Figure 2.1: Plot of the (black) spectral element basis functions according to equation (2.32) with $N = 6$ together with (red) the corresponding graph of equation (2.31).

the coefficients $a_k(t)$ from equation (2.28) are equal to the value of the solution $\phi(x_k, t)$ at the Gauss-Lobatto Legendre quadrature points. Accordingly, the discretized function is written as follows:

$$\phi_A(x, t) = \sum_{k=0}^N \phi(x_k, t) \cdot \pi_k(x) \quad (2.33)$$

2.3 Temporal discretization

For the temporal discretization, a time splitting scheme is utilized in this work that decouples the system of conservation equations of the “hydrodynamic” (the continuity and momentum equations) and the “thermochemistry” (species and energy equations) part. This splitting scheme is presented in section 2.3.1 and the thermochemistry part is discussed in more detail in section 2.3.2. The thermochemistry part is integrated with a parallel ODE-solver which is briefly presented in appendix A.

2.3.1 Splitting approach

Because of the presence of chemical source terms in the energy and species conservation equations, the time integration of the thermochemistry subsystem is performed fully implicitly using high order stiff time integration (see appendix A). In the low Mach number limit, the velocity field responds to changes in temperature or density on a slower inertial time scale. The integration of the momentum and continuity equation is performed using a high order semi-implicit splitting procedure, which leads to minimal errors in mass conservation and to a decoupled solution procedure. In order to account for the compressibility of the velocity field due to the heat produced by the exothermic chemical reactions and species diffusion, a pressure Poisson equation is derived for the “hydrodynamic pressure” (p_1), accounting for the non-zero divergence of the velocity field.

During the evaluation of the thermochemistry part, the velocity field is frozen, whereas during the call to the hydrodynamic solver all species fields, temperature and density are frozen. After each call to the thermochemistry solver, the solutions of the temperature and species mass fractions at the new time level t^{n+1} are obtained. Using these updated quantities, the continuity equation and the equation of state, one can calculate the divergence of the velocity field at the new time level t^{n+1} . The divergence of the velocity field due to chemical reaction and species mass

diffusion is

$$\begin{aligned}
 p &= \frac{\rho(\underline{x}, t)T(\underline{x}, t)}{M(\underline{x}, t)} = 1 \\
 \ln(1) &= \ln(\rho) + \ln(T) + \ln(M') \\
 &\quad \text{where } M' = \frac{1}{M} \\
 0 &= \frac{D(\ln(\rho))}{Dt} + \frac{D(\ln(T))}{Dt} + \frac{D(\ln(M'))}{Dt} \\
 -\frac{1}{\rho} \frac{D(\rho)}{Dt} &= \frac{1}{T} \frac{D(T)}{Dt} + \frac{1}{M'} \frac{D(M')}{Dt} = \nabla \cdot \underline{u} \\
 &\quad \frac{1}{T} \frac{D(T)}{Dt} + \frac{1}{M'} \sum \frac{1}{M_i} \frac{D(Y_i)}{Dt} = \nabla \cdot \underline{u}, \quad (2.34)
 \end{aligned}$$

where M is the mean molecular weight. Equation (2.34) can be evaluated using the known temperature and species mass fractions profiles obtained from the integration of the energy and species equations. For a more detailed description of the numerical scheme refer to the work of Tomboulides et al. [51, 52] and Lee [34].

2.3.2 Thermochemistry subsystem

The thermochemistry part of the code integrates the energy and the species conservation equations. During the integration of the thermochemistry subsystem, the velocity field is frozen to their values at the previous time step as mentioned in section 2.3.1. The chemical source terms in these equations introduce stiffness due to their large range of chemical time scales [33]. In order to avoid the strong time step restrictions associated with the use of explicit schemes to stiff systems, a fully implicit formulation is chosen for the integration of the thermo-chemistry part in this work.

The spatial discretization of the energy and species conservation equations, lead to a system of ordinary differential equations (ODE). In order to solve this large set of ODEs, the fully implicit, parallel solver CVODE (formerly called PVODE) [13, 6] is used. This is an ODE solver designed for large systems of equations. It applies a variable internal time step and returns the interpolated solution according to the global time step of the code. In appendix A, CVODE and its implementation to the numerical code are presented.

2.4 Code validation

The validation of the code after its extension for detailed chemistry/transport and the coupling to the fully implicit stiff ODE integrator, is accomplished with available numerical data. The validation was performed in two steps, from which the first is a validation of the chemistry part and its coupling with the implicit solver. The second step is a validation against detailed numerical data for a complex diffusion flame case. As a first step, the chemistry part of the code was validated by simulating a homogeneous (no spatial variation), constant pressure reactor and comparing the results with the corresponding code (CONP) from the CHEMKIN package. A two dimensional domain with zero-gradient boundary conditions was used for this simulation. A comparison of the heat release showed to be identical, independent of the global time step (integration time step of the DNS code) for the spectral element code. The second step was the validation against an already validated serial, two-dimensional DNS code. This numerical code was used for a number of investigations, and employs the same numerical schemes and algorithms as the three-dimensional code developed in this work. The validation case was an axisymmetric opposed jet with a nitrogen diluted oxygen-hydrogen diffusion flame, for which extensive simulation results of [18] were available and which is a case, where flow, transport and chemistry play important roles.

2.4.1 Computational set up and results

The boundary conditions used here for velocity are plug profiles. The velocities were equal in both streams and set to a value of 31.8cm/s corresponding to a Reynolds number of 200. The compositions of the two streams were 20% *vol.* H_2 diluted with nitrogen in the fuel nozzle and air in the oxidizer nozzle. The wall boundary conditions were set to no-slip conditions for the velocity on the constant temperature ($T_{wall} = 300\text{K}$), nonreactive walls of the numerical domain. Zero-Neumann boundary conditions were applied for all variables at the outflow boundary. The diameter of both the fuel and oxidizer nozzles and the separation distance are equal to 1 *cm*. The computational domain including the spectral element skeleton is shown in figure 2.2.

The three dimensional, parallel code was used to simulate the same case as in [18]. The comparison of the main variables along the axis of symmetry is shown in Figure 2.3. The comparison for the species mass-fraction agree very well and no differences can be seen. The shape of the

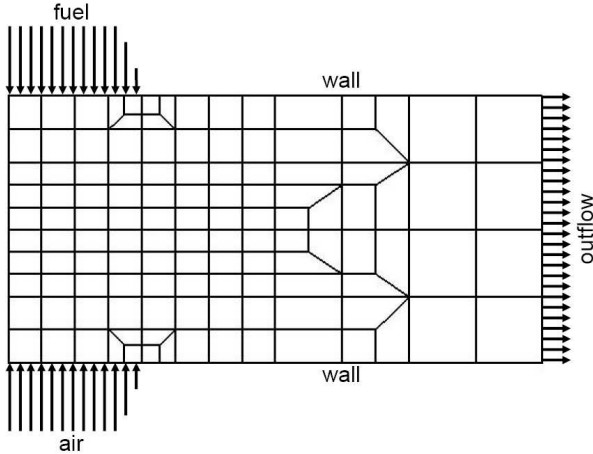


Figure 2.2: Computational domain with spectral element skeleton and qualitative velocity boundary conditions for the fuel stream, the oxidizer stream and the outflow.

temperature-curve is the same, while its maximum temperature differs by $9K$, which is a relative error of 0.6% . The small differences in the results occur due to the neglect of thermal diffusion in the three dimensional code. The small inconsistency is of negligible size and not relevant for the simulations performed within the scope of this work.

The scalability of the code was analyzed using the same set-up, but a much higher spatial resolution, in order to enlarge the problem to a size, for which the splitting of the domain on 64 processors is reasonable. A certain interval of physical time was simulated applying one to 64 processors and the time of computation was set in relation to the number of applied processors (npr). The simulated time was chosen large enough to minimize the influence of the initialization of the computational problem. Figure 2.4 shows the scalability of the code which is perfect for up to 32 processors. The simulations in this work were performed on 16 or 32 processors.

2.5 Summary

The existing single step chemistry, simple transport DNS code was extended to account for detailed chemistry and transport properties by coupling with the Chemkin library. The numerical code which is presented

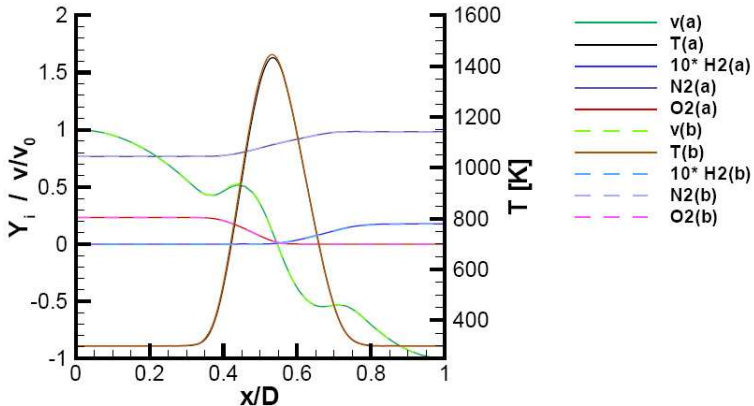


Figure 2.3: Comparison of the simulation results along the axis of symmetry of a opposed-jet for the well established 2D, serial (a) and the new 3D, parallel (b) code.

here solves the Navier-Stokes equations in the low-Mach formulation. The spatial discretization is done using spectral elements, which combines the high-order accuracy of spectral methods with the flexibility of finite element methods. A splitting approach is used for the temporal discretization, where the fluid- and the thermo-chemistry part are solved independently. The implementation of the strongly nonlinear, stiff detailed chemistry source term, is associated with numerical difficulties which are treated with a fully implicit formulation of the thermo-chemistry part of the code. The implicit integration of the large system of equations is performed using CVODE, a parallel, stiff ODE solver. The temporal discretization of the velocity part realized applying a second order semi-implicit, multi-step scheme. The code shows perfect scalability for reasonably sized problems.

The code was validated against numerical results obtained using a serial two dimensional spectral-element DNS code. In the following chapters, the application of the code on two different problems is presented: The opposed-jet simulation of the experimental opposed-jet set-up of Ciani [10], and the cellular diffusion flame set-up of Lo Jacono et al. [40].

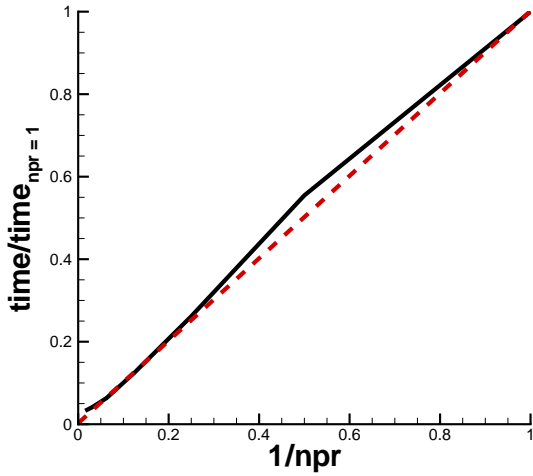


Figure 2.4: Scalability of the code for 1 to 64 processors (npr = number of processors) compared to the line of perfect scalability (red).

Chapter 3

Opposed-jet diffusion flame instabilities

The parallel spectral element code was first used to simulate N₂-diluted hydrogen/air flames in the axisymmetric opposed-jet burner used by Ciani [10] to study diffusion/edge flame transitions. The aims of this work were to (a) validate the code against detailed experimental data (two-dimensional velocity and species concentration profiles obtained with non-intrusive laser diagnostic techniques), and (b) to explain some unexpected transitions observed in the experiments.

The chapter starts with a short overview of the extensive literature on the use of opposed-jets in combustion studies in section 3.1. The experimental set-up is then briefly described in section 3.2. In section 3.3 the numerical predictions are compared with the experimental results and in section 3.4 the findings are summarized.

3.1 Opposed-jet flames

The opposed-jet or counter flow burner is an important experimental configuration typically used to study aerodynamically stabilized, strained, non-premixed and premixed flames. This configuration offers the advantages of flames stabilized away from the burner boundaries. Furthermore, the flame is nearly one dimensional which greatly facilitates modelling. The simulation results of such strained laminar diffusion flames is the basis for the widely used flamelet combustion model [46].

An opposed-jet burner (shown schematically in figure 3.1) consists of two coaxial aligned opposed tubes or contoured nozzles with a typical separation distance of the order of the inner-tube diameter. Fuel and oxidizer streams are impinging on each other, forming a stagnation surface. Along this region, mixing occurs and, if ignited, a flame can be stabilized. Its location relative to the stagnation plane is a function of the stoichiometric proportions and the diffusivity of the fuel and oxidizer, and, in general, does not coincide with the stagnation plane of the flow field.

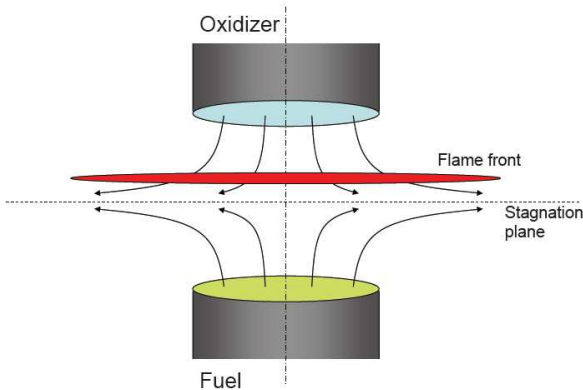


Figure 3.1: Schematic illustration of an opposed-jet diffusion burner

In most of the investigations of non-premixed opposed-jet flames, the focus is on the disk-shaped strained diffusion flame, stabilized between the two nozzles. Almost fifty years ago, another ring-shaped flame type referred to as “broken” or locally extinguished flame, was observed by Potter et al. [48]. This flame type, which is more generally referred to as an edge flame, continues to attract considerable interest.

The recent review by Buckmaster [3] discusses the nature, structure and importance of diffusion and premixed, laminar and turbulent edge flames in different configurations, as well as the theoretical, experimental and numerical work that aided in the understanding of these flames.

Pellett et al. [45] presented an extensive investigation of the fuel and oxidizer velocity limits for the stabilization of diffusion (disk-shaped) and edge (ring-shaped) flames of nitrogen diluted hydrogen and air opposed-jet flames. It was found that for each fuel-stream composition a range of flow rates for the two jets exist, in which hysteretic transitions (“blow-off” and “restoration”) between the two flame structures can occur.

Motivated by the work of Pellett et al. [45], direct numerical simulations with detailed chemistry and transport were performed by Lee and Frouzakis et al. [35, 19, 20]. In their two-dimensional, axisymmetric configurations, cold walls were used to constrain the flow between the two nozzles and provide well-defined boundary conditions. For fixed fuel and oxidizer compositions, the range of flow rates over which the diffusion and edge flames are stable was numerically determined, predicting the co-existence of the two flame types over an extended range and the associated hysteretic transition between the two flame types.

3.2 Experimental set-up

In order to efficiently study the effect of fuel type, dilution, flow rate and burner geometry on the stability of counterflow edge and diffusion flames in detail, a burner, similar to the one analyzed by Pellet [45], was constructed by Ciani [10, 11]. Experiments with pure and diluted hydrogen and methane were carried out.

The burner consisted of two steel tubes in a vertical, coaxial counter-flow configuration, contained in a rectangular housing with quartz windows for optical access. Three burner dimensions were investigated, using tubes with inner diameters of $d = 2.7, 5.0$ and 10.0 mm. The tubes were separated by a vertical gap, which was equal to the tube diameter. The tubes length was fifty times the diameter, which should result in parabolic velocity profiles at the nozzle exit, as verified by particle image velocimetry measurements of the velocity at the exit of isolated (i.e. not in a counterflow configuration) nozzles. At the plane of the tube exit, water-cooled brass discs were attached in order to provide well-defined boundary conditions and permit comparison with the numerical simulation results; the diameter of the brass discs was $D=72.0$ mm. During the experiment, the cooling water temperature was kept constant at $T = 338K$ in order to avoid condensation of the water vapor generated in the flame. The temperature of the brass discs was measured with a thermocouple, which was installed in the discs, $1.5mm$ away from the gas phase. According to these measurements, the temperature variation of the disc along the radius, due to the combustion, was less than $10K$. The flows and their dilution were adjusted using computer-controlled mass flow controllers and the fuel, either pure or diluted with nitrogen and the overall flow velocities and the degree of fuel dilution were specified via a LabView program. The experiments were performed with fuel introduced in the upward flowing bottom tube and oxidizer in the opposite, downward flowing upper tube. The gas

temperature at the nozzles was measured with a thermocouple inserted immediately after the extinction of the flame. For the most typical flames the measured temperature of the inflowing gases was around $323K$. The housing was flushed with a slow, diffuse stream of nitrogen to purge the ambient air and prevent uncontrolled combustion of excess fuel.

The stabilized flames were analyzed using three complementing measurement techniques: Planar laser induced fluorescence (PLIF) and chemiluminescence in the visible and the UV-range were used to characterize the flame structure by the OH radical distribution, particle image velocimetry (PIV) was used to obtain the two-dimensional velocity field under cold and reactive conditions and the Raman scattering was used to measure the distribution of the major species (O_2 , H_2 , H_2O and N_2) which were used to calculate the temperature.

The extensive parametric study of Ciani [10] consists of measurements for large numbers of fuel and air velocity combinations for two different fuels (methane and hydrogen at different dilutions).

Particular attention was given to the stability diagrams, where the velocity range within which a diffusion or an edge flame could be stabilized were determined. Such a stability diagram for the numerically investigated fuel composition of 50% *vol.* hydrogen in nitrogen studied here, is displayed in figure 3.2. The diffusion flame was stable for flow velocities in the region delimited by the curves marked by filled symbols. The lower curve is defined as the minimum air velocity required to keep the diffusion flame in the area between the two cooling disks. For lower air flow velocities, the flame burned inside the air tube, which was a limitation of the setup used here. The edge flame could be shown to exist for the velocity range between the two curves marked by open symbols.

The lower stability boundary curve of the edge flame is characterized by a well defined relative minimum at $u_c \approx 2.2 m/s$, which divides the line in two parts. For $u_f < u_c$ a reduction of the air velocity resulted in a movement of the edge flame towards the nozzle axis and after crossing the stability boundary, restoration of the diffusion flame could be observed. For $u_f > u_c$ a reduction of the air velocity below the lower edge flame stability boundary, resulted in the quenching of the edge flame, even though a diffusion flame was also stable at these conditions.

The overlapping crosshatched region marks the range where both flame types were stable. In this region, transitions from one flame type to the other could be induced by perturbing the flame using bluff bodies.

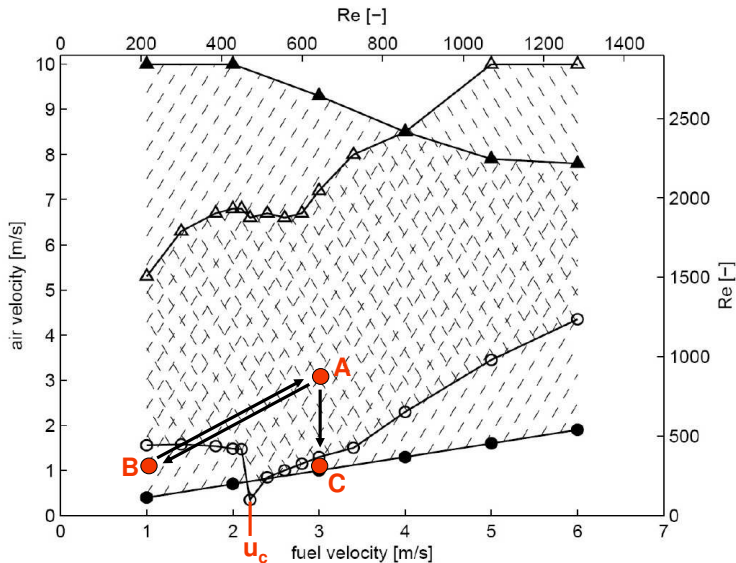


Figure 3.2: Stability diagram for diffusion and edge flames for 50% *vol.* H_2 in N_2 on the fuel side and air on the oxidizer side. The diffusion flame is stable for flow velocities in the region delimited by filled symbols, and the edge flame in the region delimited by open symbols [10, 11].

3.3 Simulation results

The focus of the numerical investigations is the burner geometry with inner tube diameters of $d = 5.0 \text{ mm}$ and a fuel stream consisting of 50% *vol.* hydrogen in nitrogen. With these conditions, stain rates high enough for local flame extinction can be achieved while the flow remains laminar. These local flame extinction around the axis of symmetry eventually results in the transition from the disk-shaped diffusion flame to a ring-shaped edge flame.

The numerical investigations presented here are motivated by a disagreement of the location the flame on the jet axis in the experimental and the numerical results of [10] and the different behavior observed for u_f smaller or larger than u_c discussed in the previous section.

The simulations presented in [10] were performed using a serial code which is similar to the one used in this work. Since the length to diameter ratio of the coaxial tubes of the burner is large ($L/d = 50$), parabolic inflow

velocity profiles were assumed at the exits of the fuel and oxidizer nozzles. The axisymmetric computational domain with the same dimensions as the experimental one, was discretized into 308 spectral elements; eighth-order interpolating polynomials were used in each direction. Fuel and air entered the domain at $323K$. The cold, non-reactive disks were considered to be at a constant temperature ($T = 338K$), and the no-slip and zero-flux boundary conditions were enforced for the velocity and species, respectively. Zero-Neumann boundary conditions were imposed $5.4 d$ away from the symmetry axis.

These simulations showed reasonable qualitative agreement, as can be seen in figure 3.3, where the experimental and numerical result for the OH concentration of a diffusion flame with average inlet-velocities of $3 m/s$ of the fuel and the oxidizer stream, are plotted. The experimentally accessible part of the burner is indicated in the plot of the simulation result for easier comparison.

The main difference between the experiment and the simulation result

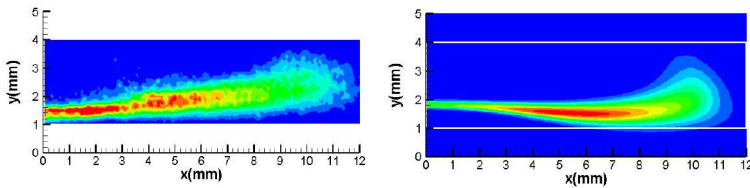


Figure 3.3: Concentration of the experimental (left) and simulation (right) OH concentration in a opposed-jet diffusion flame with the conditions of point A on figure 3.2: fuel and oxidizer of 50% *vol.* H_2/N_2 mixture and air with equal average inlet velocities of $3 m/s$ for both streams [10].

can be seen close to the axis of symmetry, where the location of the simulated flame zone is closer to the center of the domain and the flame is very thin relative to the experiment. Associated with this mismatch, is a difference in the shape of the flame, since the flame location further away of the axis is similar in experiment and simulation. Along the radial direction, the simulated flame bends downwards, while the experimental result shows an almost straight flame extending towards the center of the burner. The numerical investigations performed here will reveal that this difference is due to the assumption of parabolic inflow velocity profiles at the nozzle exits.

A parabolic profile would be the correct assumption for the velocity profile in the nozzle of a free jet. For an opposed-jet configuration, where the flow

is deflected just after the nozzle exit by the stagnation plane, the assumption of the parabolic inlet profile cannot always be satisfied. The presence of a stagnation plane and due to it, the baffle of the jets influences the velocity profile at the opposed-jet nozzle exit. Additionally, there is an influence of the geometry of the burner. The circular disks attached to the nozzles in order to provide well-defined boundary conditions for the simulations, result in the formation of recirculation zones attached to the upper and lower disk. These recirculation zones influence the location of the stagnation plane and shift it towards the upper or lower nozzle. For some combinations of fuel and air velocities, the stagnation plane can be located on either side, but can no longer be stabilized halfway between the nozzles, even for flows with equal momenta at both nozzles. The sudden change of the location of the stagnation plane was observed when the fuel velocity was kept constant and the air velocity was slowly varied. This “switching” was associated with a small hysteresis. This bi-stability is illustrated in figure 3.4. The large recirculation zones, formed close to the lower (left image) or upper (right image) disk, force the total gas inflow to exit through a rather narrow region in close vicinity to one of the disks. The stagnation plane bi-stability has a strong influence on the velocity

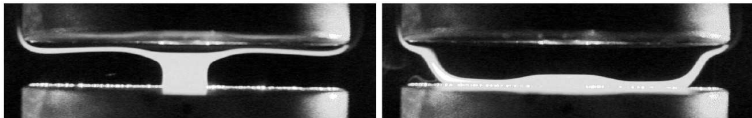


Figure 3.4: For a wide range of inlet-velocities, the stagnation plane is located either on the fuel or on the oxidizer side as visualized here for the cold flow seeded with oil droplets [10].

profile at the nozzle exit, especially, to the nozzle where the stagnation plane is very closer to.

The velocity boundary condition issue at the nozzle exits can be addressed by specifying experimentally determined velocity profiles, requiring velocity measurements for all the conditions considered. Here, we opted for another solution. The computational domain was extended two nozzle diameters into the tubes, allowing for the flow to adjust freely at the nozzle exits. On the inflow boundary within the tubes, parabolic boundary conditions could be safely imposed. Figure 3.5 shows the extended domain, including the spectral elements. Within each element, the variables are expanded using sixth-order polynomials. The new computational mesh consists of 552 elements and is locally refined at the edges of the nozzles.

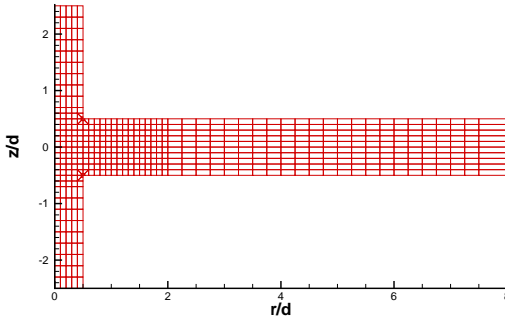


Figure 3.5: The extended domain includes $2d$ of each of the tubes and it expands $8d$ in radial directions. It consists of 552 spectral elements.

The extended domain was first used in the simulation of an edge flame with a 50% *vol.* hydrogen fuel stream and air, both with average inlet-velocities of 3 m/s . Figure 3.6 shows the calculated velocity profiles at the fuel nozzle (solid line) and the air nozzle (dashed line) in the axial (red) and radial (blue) direction in the presence of a diffusion flame. For these conditions, the stagnation plane is located very close to the fuel nozzle and therefore the total flow of the fuel nozzle is forced to exit through a rather narrow region in the close vicinity of the lower disc.

Especially close to the edge of the fuel nozzle, very high velocities in both axial and radial direction occur, due to the stagnation plane which deflects the flow in the radial direction. The maximum axial velocity with the parabolic velocity profile is twice the average velocity and the maximum is on the axis of symmetry. The simulated axial inlet velocity profile shows a constant velocity of slightly less than the average of 3 m/s in a large region around the axis but a large increase in velocity very close to the edge of the nozzle, where a maximum of more than 4.6 m/s is reached. The radial velocity profile at the air nozzle is very close to the parabolic profile (green, dash-dotted line), since the distance of the nozzle to the stagnation plane is much larger.

Figure 3.7 compares of the distribution of fuel, oxidizer and product (water) of the Raman scattering measurements (negative r/d axis) with the computational results (positive r/d axis) for these conditions. The experimentally accessible region was $-0.3 < z/d < 0.3$ and $0 < r/d < 2.4$ for a coordinate system with its origin in the center of the burner.

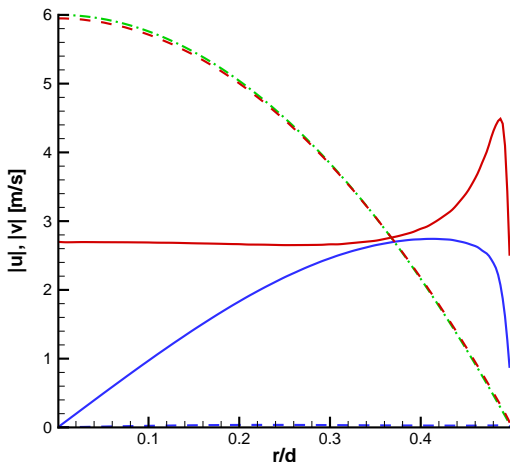


Figure 3.6: Normalized, calculated radial velocity profiles at the nozzle exit of the fuel (solid lines) and air (dashed lines) nozzles of an opposed-jet diffusion flame with average inlet-velocities of 3 m/s on both sides. The colors are red for the axial- and blue for the radial velocity. The green line indicates the parabolic profile.

For easier comparison, this region is also indicated in the plots of the simulation results, where the whole region between the two circular discs until $r = 3.3 d$ and a small part of the inflow tubes are plotted.

The temperature distribution (figure 3.7 (a)) shows very good agreement not only for the high temperature zones, but also for the low temperature region in the recirculation zone. The maximum temperature is predicted slightly higher than in the experiment. This issue is discussed in more detail below, together with figure 3.8. In figure 3.7 (b), the comparison of the hydrogen mole fraction does not provide much information, since the concentration in the experimentally accessible region is only marginal. The slightly increased concentration between $r/d = 0.5$ and $r/d = 1.5$ at $z/d = -0.3$ is equal in the experiment and the simulations. The profiles of oxygen mole fraction (figure 3.7 (c)) from Raman scattering with the simulated results shows very good agreement. The small difference in the penetration of the oxygen along the jet axis towards the fuel nozzle can be attributed to the insufficient spatial resolution of the Raman

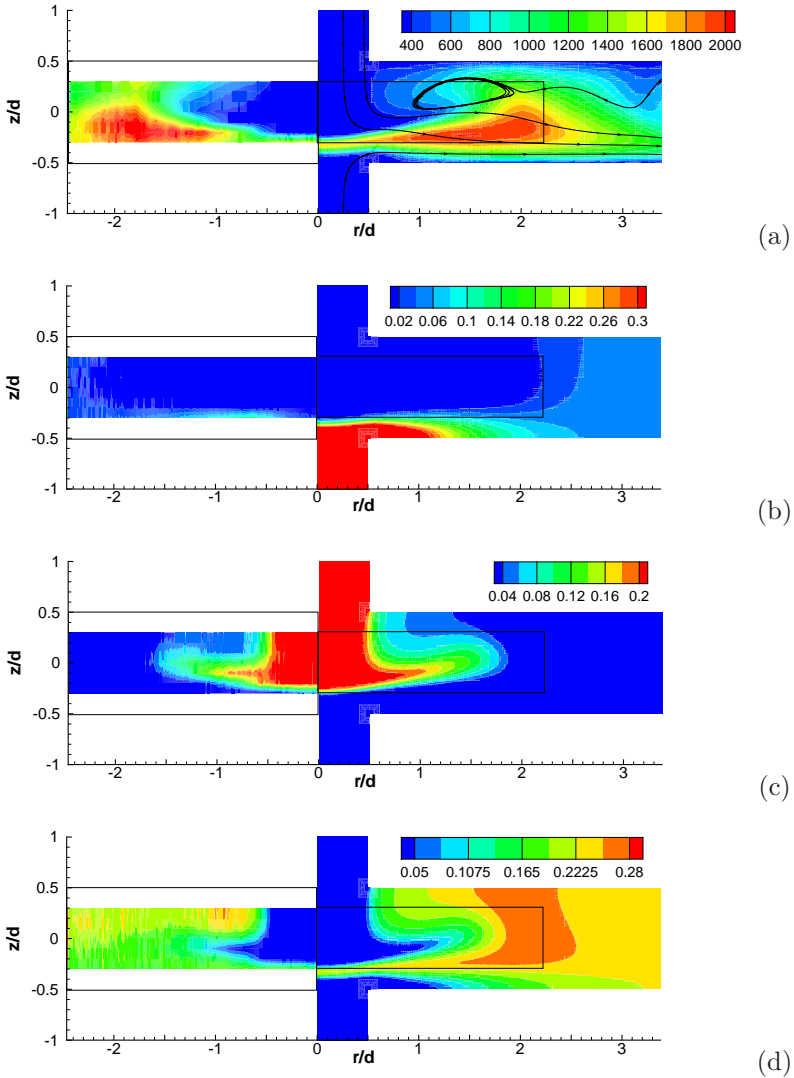


Figure 3.7: Experimental (left) and numerical (right) major species mole fractions and temperature in the diffusion flame with inlet-velocities of 3 m/s : (a) temperature, (b) hydrogen , (c) oxygen, (d) water.

scattering measurements in the axial direction (the spatial resolution in radial direction is much larger). The comparison of the water distribution (figure 3.7 (d)) shows a similar offset in the axial direction as for the oxygen field, but the agreement of the low water concentrations is very good. The location of high water concentration close to the air nozzle, as it is documented in the experimental result, can not be seen in the simulation results. The computed water mole fraction has its maximum close to the reaction zone, and from there, the water is convected towards the upper disk. The experimental result shows an accumulation of water away from the reaction zone to higher values, which is not physical. This high water concentration might be a result of the initial conditions, which was trapped in the closed recirculation zone close to the air nozzle and could not be convected away.

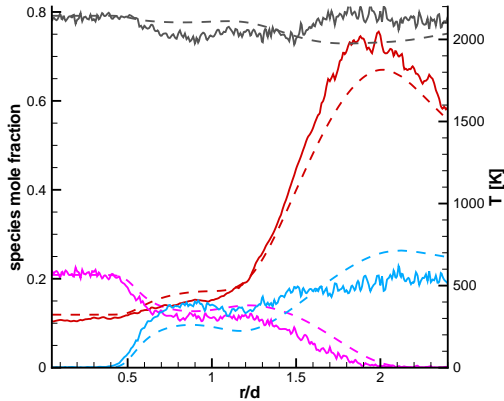


Figure 3.8: Comparison of the experimental (solid) and numerical (dashed) radial distribution of species mole fractions for N_2 (grey), O_2 (purple) and H_2O (blue) and temperature (red) in the center of the burner, in case of a diffusion flame for inlet velocities of 3 m/s

In figure 3.8, the profiles of the major species mole fractions and temperature in the radial direction are compared along the center line of the burner ($z/d = 0.0$). Between the nozzles ($r/d < 0.5$), the experimental and numerical values are in good agreement. The oxygen profiles follow

the same trends with a region of almost constant, high concentration in the region between the nozzles and another region of almost constant concentration before the point of steep temperature increase ($0.8 < r/d < 1.3$). There is good quantitative agreement along the profiles as well as for the point of fully consumed oxygen at $r/d \approx 2.0$. The water concentrations follows the same trends as well, but in the simulation, the concentration is underestimated prior to the flame and over-estimated in the flame, compared to the experiment. The water concentration is under-predicted in the region $0.5 < r/d < 1.5$, this due to the above described discrepancy in the experimental obtained water distribution and the simulations. The difference in the reaction zone might be due to the differences in the temperature discussed below. The maximum temperature is higher in the experimental results, but until the high temperature zone, the two lines are in good agreement. Especially the sudden bend in the graph at $r/d \approx 1.25$, which is an indication for the flame location, is equal in experiment and simulation. The temperature is not directly measured in the experiment, but evaluated from the temperature dependent signal of the nitrogen. This iterative process is accurate for lower temperature and is known to be less accurate for temperatures around and over $2000K$ (see [1]). The evaluated temperature influences the measurements of the other species, since their apparent scattering cross section is temperature dependent.

In figure 3.9 the stream-lines of the flow field corresponding to the diffusion flame are plotted together with the oxygen concentration. The streamlines show clearly the large recirculations zone next to the upper nozzle. The main radial flow is close to the lower disk, the stagnation plane is below $z/d = -0.3$ and therefore below the experimentally accessible region for the Raman scattering measurements.

It was found experimentally (figure 3.2), that for the same conditions an edge flame can also be stabilized. The same behavior was observed numerically. For the edge flame simulation, the cold flow was ignited by introducing a hot spot away from the jet axis. The comparison of the experimental results with the simulation results of this edge flame is presented in figure 3.10.

Figure 3.10 (a) shows agreement in the location of the high temperature field as well as of the low temperature distribution. The measurements show higher temperatures similar to the above presented comparison for the diffusion flame (figure 3.7 (a)). The comparison of hydrogen and oxygen concentration (figure 3.10 (b) and (c)) shows good agreement for the accessible area, but since the stagnation plane is very close to

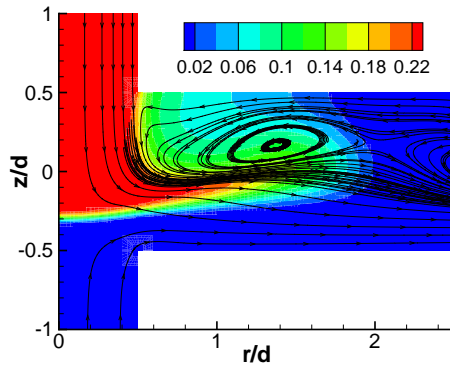


Figure 3.9: Streamlines for the diffusion flame case of point (A) in figure 3.2 colored with the iso-contours of the oxygen concentration.

the fuel nozzle, the interesting effects take place outside this region. The experimentally measured water mole fraction distribution shows, similar to the result for the diffusion flame, high concentration close to the air nozzle, while the simulation shows a more physical distribution with the maximum concentration close to the reaction zone. As for the diffusion flame, this difference might be due to different initial conditions and the recirculation zone, which prevents convection of the initial gas composition.

The comparison of the concentration of the main species in the radial direction along the burner centerline shows good quantitative agreement of experiment and simulation (figure 3.11). As in figure 3.8, the agreement is very good in the area between the nozzles. The oxygen profiles are qualitatively similar. They display a sudden drop around $r/d = 0.4$ and has a zone with almost constant low concentration for $0.7 < r/d < 1.5$ followed by complete consumption. The quantitative agreement is also good with a constant offset in the low concentration zone. The concentration of the water is, similar to the diffusion flame (figure 3.8), under-predicted in the zone before the flame and over-predicted in the flame zone. The qualitative agreement of the temperature is good with a sudden bend at $r/d = 0.4$ and the maximum temperature at $r/d = 1.8$. Good quantitative agreement is obtained for $T < 1500K$, but the experimental evaluated maximum temperature is significantly higher.

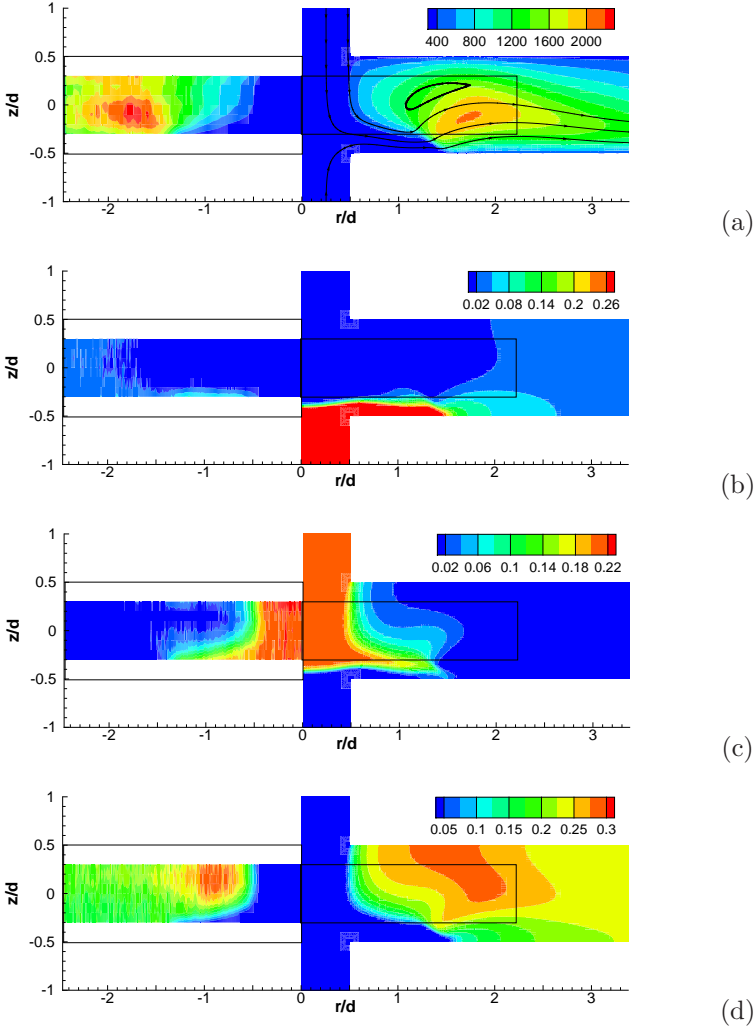


Figure 3.10: Experimental (left) and numerical (right) major species mole fractions and temperature for the case of an edge flame for inlet-velocities of 3 m/s : (a) temperature, (b) hydrogen, (c) oxygen, (d) water

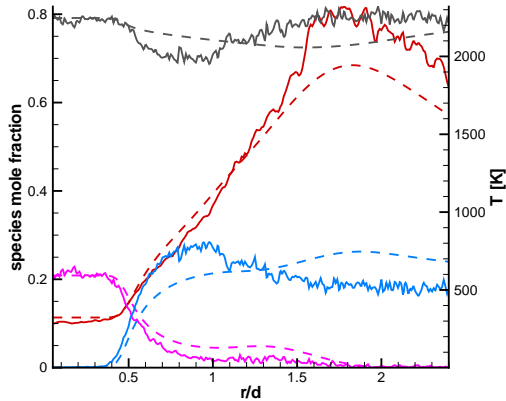


Figure 3.11: Comparison of the experimental (solid) and numerical (dashed) radial distribution of species mole fractions for N_2 (grey), O_2 (purple) and H_2O (blue) and temperature (red) in the center of the burner, in the diffusion flame with inlet-velocities of 3 m/s

As described above, the experimentally evaluated temperature is less accurate for higher temperatures. Differences in the temperature fields can also be seen in the temperature iso-contour plot in figure 3.10, where the high temperature zone extends further towards the upper disk, where the presented data is extracted.

Additional investigations were dedicated to the transient behavior of the edge flames close to the stability boundary for low air velocities (see figure 3.2). The region of $u_{air} < u_c$ was investigated first, starting from the above described edge flame with fuel and air velocities of 3 m/s (figure 3.2, point A). As expected from the stability diagram, an impulsive reduction of both velocities to 1 m/s (figure 3.2, point B) resulted in restoration of the diffusion flame. The lower velocities allowed the edge flame to propagate all the way to the burner axis, where due to the lower strain, restoration of the diffusion flame occurred. Starting from the obtained diffusion flame, a sudden increase of both velocities to their original values of 3 m/s resulted in a visibly strained, but stable diffusion flame. This was predicted from the stability diagram of figure

3.2. The velocity combinations for which this bi-stability could be shown experimentally is indicated with the crosshatched region in the stability diagram.

In figure 3.12, the simulated OH concentrations of the above described flames are displayed.

The lower stability boundary of the edge flame of figure 3.2 in the

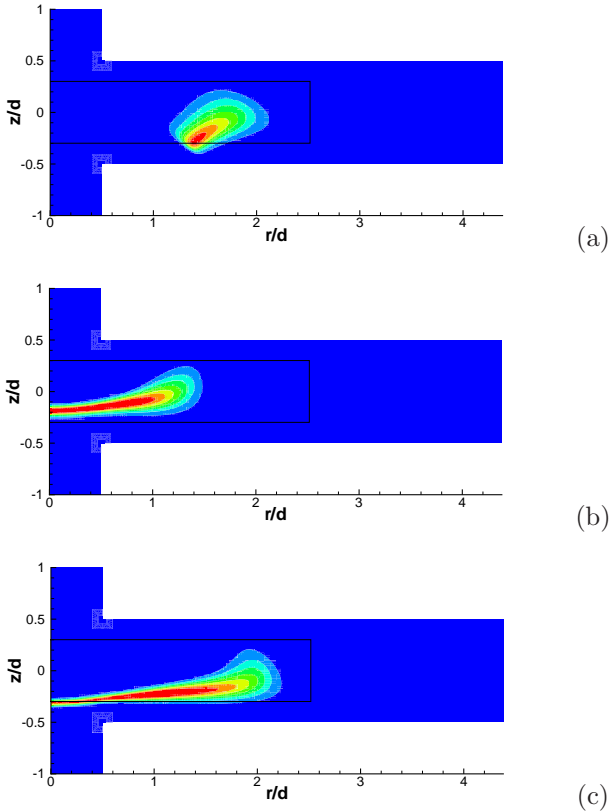


Figure 3.12: Simulation iso-contours of the mass fraction Y_{OH} for the edge flame of point A (a), the diffusion flame of point B (b) and the diffusion flame of point A (c) of figure 3.2.

region of $u_{air} > u_c$ was also analyzed starting from the edge flame of point A in the above mentioned figure. The average air velocity was

impulsively reduced to 1 m/s , while the velocity at the fuel nozzle remained unchanged. These flow parameters correspond to a region in figure 3.2 (point C), where only the diffusion flame is stable. However, instead of restoration of the diffusion flame, the flame extinguished, in agreement with the experimental observations. Figure 3.13 shows the temporal change in the flame as response to the impulsive reduction of the average air velocity from 3 to 1 m/s .

The analysis of the simulation results revealed the reason for the extinction of the edge flame: The decrease of the air velocity resulted in a sudden shift of the stagnation plane away from the fuel nozzle towards the air nozzle, as the streamlines in figure 3.13 indicates. The flame front did not propagate fast enough to follow the fuel flow, and continued for a short time to burn close to the fuel side. As it was deprived of oxygen, it could only be sustained until the oxygen remaining around it was consumed, leading finally to flame extinction.

A simulation for the same configurations as above, with a gradual reduction of the air velocity did not result in extinction. The maximum flame temperature in the simulation, dropped from 2018K to 1740K and a small reaction zone attached to the upper wall was sustained. Experiments where the air velocity was reduced in small steps showed the same behavior. The resulting edge flame with averaged fuel and air velocities of 3 and 1 m/s is shown in figure 3.14.

The temperature iso-contour plot (figure 3.14 (a)) shows the small reaction zone close to the upper wall. The hydrogen plot (b) and the oxygen plot (c) indicate that the stagnation plane is located very close to the air nozzle. On the jet axis, the hydrogen stream penetrates into the air nozzle. The water vapor concentration (d) shows that the flame is located very close to the upper wall. The location of the stagnation plane inside the air nozzle and the associated high velocities at the edge of the nozzle make the restoration of a diffusion flame impossible. The propagation of the flame towards the jet axis is impeded by the high gas velocities despite the combustible mixture of fuel and oxidizer, since the gas velocity exceeds the laminar flame speed of the given mixture.

3.4 Conclusions

The structure and dynamics of diluted hydrogen/air diffusion and edge flames stabilized in an opposed-jet burner were studied with a combination of laser diagnostics and detailed numerical simulations. It could be shown, that the simulation results agree well with the experimental when

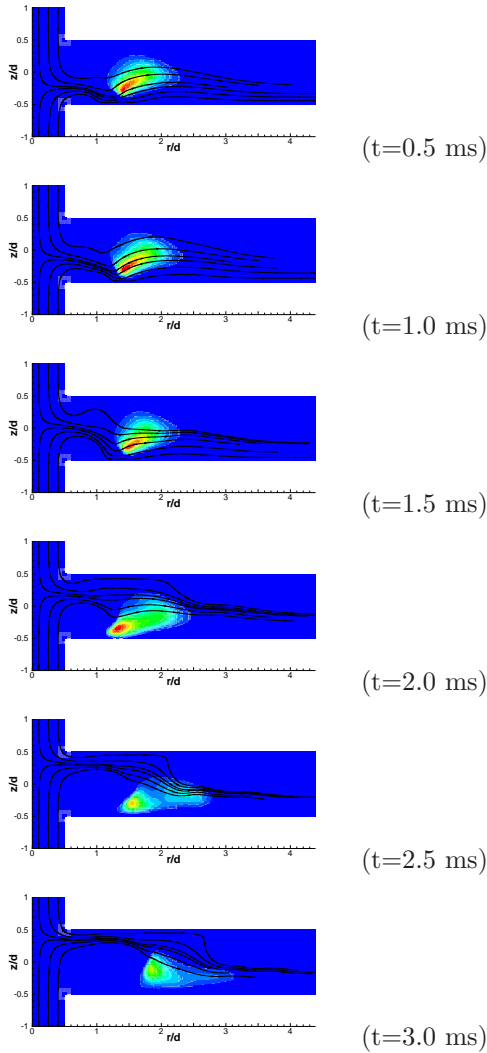


Figure 3.13: OH mass fraction of a 50% *vol.* H_2 - air opposed-jet edge flame, where the air velocity was suddenly changed from 3 to 1 *m/s* at $t=0.0$. Streamlines illustrate the flow-field.

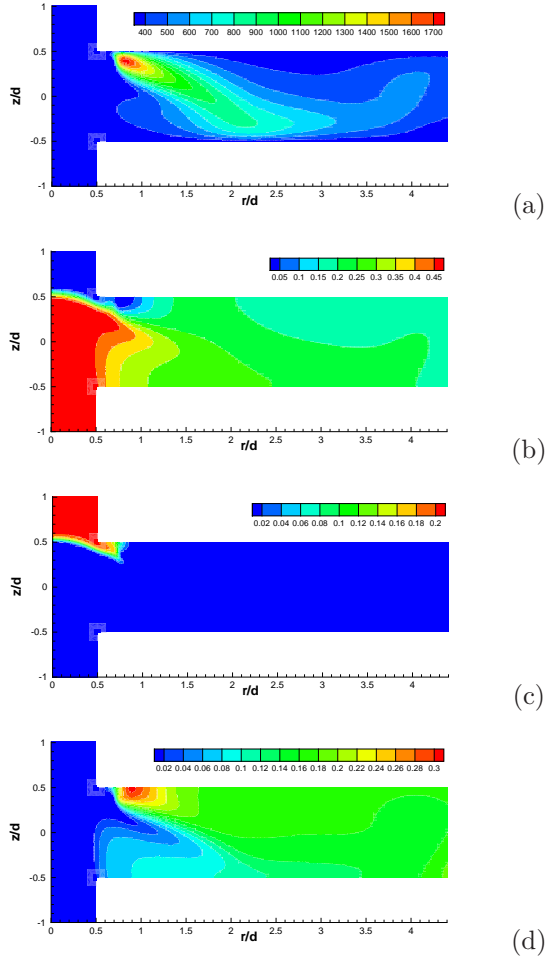


Figure 3.14: Temperature and major species mole fractions for the case of an edge flame for inlet velocities of 1 m/s (oxidizer) and 3 m/s (fuel): (a) temperature, (b) hydrogen, (c) oxygen and (d) water.

the computational domain is extended $2.5 d$ into the nozzles. This is due to the influence of the stagnation plane if located close to one of the nozzle. This can lead to complex velocity profiles which differ strongly from the parabolic profile imposed in earlier simulations.

Good quantitative agreement of experimental and simulation results could be seen for temperature as long as $T < 1500$. Also the mole fraction of the major species agreed well between experiment and simulation with the exception of the water concentration field, which shows significant differences.

In addition to the comparison of edge and diffusion flames, the transient behavior of the edge flame close to its lower stability limit in the fuel and air velocity plane (figure 3.2) was analyzed. The focus was on the differences between the right and the left hand side of the local minimum of the lower edge flame stability line at $u_c = 2.2 \text{ m/s}$. It could be shown, that the behavior is completely different for fuel velocity below u_c , where a reduction of the air velocity leads to the restoration of a diffusion flame, than for fuel velocity larger than u_c , where the edge flame cannot propagate towards the jet axis.

For higher fuel velocities, there is an additional phenomenon related to a reduction of the air velocity. Depending on whether this reduction is gradually sudden, the edge flame is either sustained or extinguished. This behavior is related to the location of the stagnation plane, which shifts from the fuel to the air nozzle due to the reduction of the air velocity. If the stagnation plane suddenly flips from one side to the other due to a sudden change in air velocity, the flame is extinguished. For slow changes in the air velocity, the edge flame is sustained despite a considerable reduction of reaction intensity.

Chapter 4

Cellular jet flames

In this chapter, the numerical study results of cellular flame structures in jet-diffusion flames close to extinction are presented. The computational investigation is guided by the experimental work of Lo Jacono [38].

The chapter is structured as follows: The experimental apparatus, the applied measurement techniques and the results of Lo Jacono are presented in section 4.1. Section 4.2 presents the computational set-up, focusing on the mesh and the initial and boundary conditions. In section 4.3, the computational results are presented and discussed. Finally, section 4.4, summarizes the main observations.

4.1 Experimental set-up and measurement techniques

The test rig used for the experimental investigations was used for a number of experimental studies at the Swiss Federal Institute of Technology in Lausanne (EPFL). Füre [22] investigated instabilities in reacting jets applying this test facility. His investigations of oscillating flames, cellular flames and Kelvin-Helmholtz instabilities initialized further experimental and numerical studies of thermo-diffusive instabilities in diffusion flames (Lo Jacono [40], Frouzakis et al. [21]).

The test rig consists of a burner (see figure 4.1) and individually controlled flow of gases (fuel, oxygen and inert). The gases are then passed through a seeder, which is used to seed the gases in order to enable LDA measurements of the flow field in the jet. The mainly axial perturbation

induced by the seeder and the flow controllers are afterwards damped with a sound muffler, an additional honeycomb flow straightener and turbulence screens. The jet has a contoured, axisymmetric nozzle with an overall contraction ratio of 100:1. With this configuration, the flow fluctuations at the jet exit were reduced to the point of producing steady laminar flows up to $Re = 1700$. The jet is oriented vertically upwards and the nozzle diameter is $d = 7.5 \text{ mm}$. Around the fuel jet, the oxidizer is supplied through a porous sintered metal plate of diameter $D = 75 \text{ mm}$, large enough to avoid any disturbance due to external flows. The co-flow velocity profile at the exit was shown to be uniform.

The velocity of the jet was measured by Laser Doppler Anemometry (LDA). These measurements were made for the cold flow, as well as for the flow including the influence of the burning flame. One of the disadvantages of this measurement technique is that the flow must be seeded, which is in general difficult for the low flow velocities of the presented cases and it is not possible at all for the co-flow region, because of the porous plate which would trap all the particles. Therefore, the LDA results are restricted to the region of the jet. Measurements in the shear-layer region are difficult to obtain, since the distribution of the particles there depends on the flow characteristics. For the available results of the shear-layer velocities, a bias is introduced due to the non-uniform distribution of the particles as described in [22]. It was found that this bias did not play a significant role for the measurement of the initial vorticity thickness. For accessibility reasons, the LDA measurements were performed 1 mm above the nozzle.

The shape and characteristics of the flame were analyzed using streamwise integrated chemiluminescence emission images, recorded from above the flame tip. Figure 4.1 shows a schematic and a photograph of the experimental setup. Figure 4.2 shows examples of the results of the LDA and the chemiluminescence measurements.

From the chemiluminescence images, the number of cells in the azimuthal direction, defining the cellular mode of the flame, is determined. The experimental investigations focused on the formation of different cellular modes for different jet and co-flow compositions and jet velocities. Two parametric studies were performed. In the first one, the composition of the jet (fuel) and co-flow (oxidizer) streams were varied by dilution with CO_2 , while the jet and co-flow velocities were kept fixed. The second study focused on the effects of the variation of the jet composition and the jet velocity with fixed co-flow parameters. The results of the two investigations together with the documented relation of the cellular mode

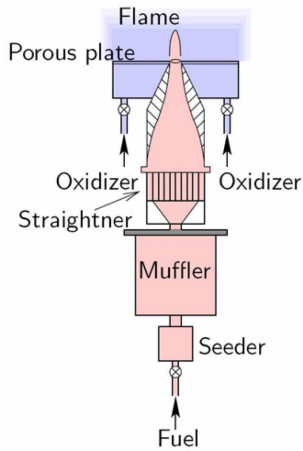
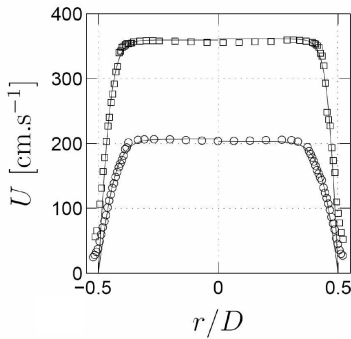
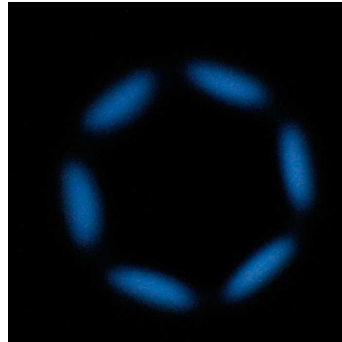


Figure 4.1: The jet burner in (left) a schematic drawing and (right) a side view (showing the porous plate).



(a)



(b)

Figure 4.2: (a) Typical velocity measurements from the LDA apparatus, taken 1 mm above the nozzle exit. (b) Photograph of the flame from the top showing the integrated chemiluminescence of a six-cell cellular jet-diffusion flame [38].

with the jet velocity profile are presented next.

4.1.1 Experimental Results

The first study (study *A*) published in [40] considers different hydrogen and oxygen dilutions in the jet and co-flow streams, respectively. The velocities of the two streams were kept fixed at $u_j = 76 \text{ cm/s}$, $u_c = 4 \text{ cm/s}$, where u_j and u_c are jet and co-flow velocities, respectively. The

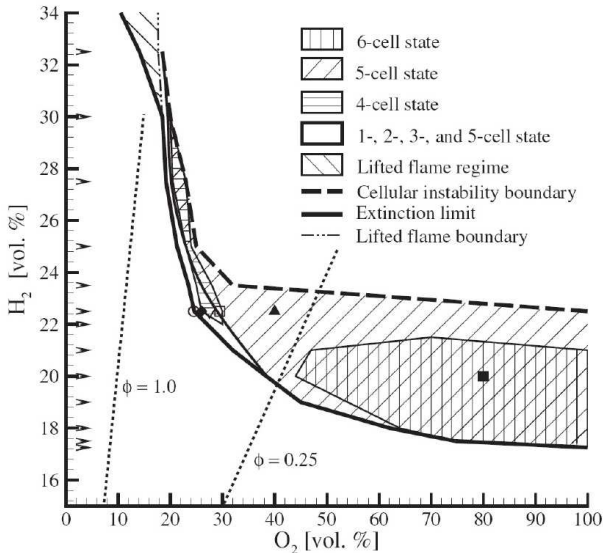


Figure 4.3: Extinction limit and boundaries of different cellular instabilities observed for CO_2 diluted, H_2 - O_2 jet diffusion flames. The centreline fuel velocity is $u_j = 76 \text{ cm/s}$ and the co-flow velocity is $u_c = 4 \text{ cm/s}$. [40]

results of this study are summarized in figure 4.3. Above the dashed line a strongly burning contiguous flame is observed, while below the solid line, no flame could be established. In the concentration range between these two lines, cellular flames could be stabilized. For some conditions, the coexistence of different cellular modes was reported. In the regions with different stable cellular modes, mechanical perturbation of the flame would in some cases lead to transition to a different cellular mode (in the experiment the flame was perturbed using a bluff body). The change of

the external parameters often resulted in the extinction of the flame, since in the investigated regime, the flame is very weak and close to extinction anyway. A flame could only be stabilized in a small region above the nozzle. When the flame was lifted too much, extinction was inevitable. In such cases, a bluff-body could be used to stabilize the flame and to move it back towards the nozzle, where it could be again stabilized.

The resulting cellular modes are presented in figure 4.4. These cellular modes were obtained at a fixed jet fuel composition with $X_{H_2} = 0.225$ (where X_{H_2} is the hydrogen mole fraction) and varying oxygen mole fractions above the extinction limit of $X_{O_2} = 0.232$ (both streams were balanced with CO_2). These images were taken with a digital camera pointed at the flame from the downstream jet axis. The colors are related to the intensity of the chemiluminescence, integrated in the streamwise direction over the entire length of the flame. The flames with lower number

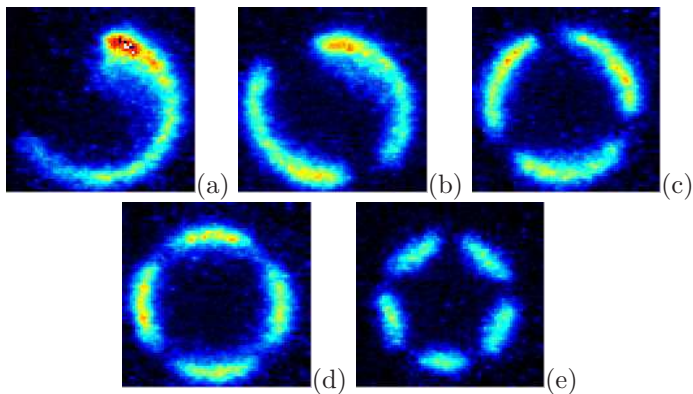


Figure 4.4: Integrated passive chemiluminescence pictures from the top of the jet burner for the cellular modes of figure 4.5 [40]. Fuel and oxygen mole fractions are $X_{H_2} = 22.5$ and $X_{O_2} = 23.2$, respectively and the velocities are $u_j = 76 \text{ cm/s}$ and $u_c = 4 \text{ cm/s}$.

of cells or higher cellular wave numbers (see below), rotated around the jet axis in either the clockwise or counterclockwise direction, depending on the initial conditions. The flames with three or less cells exhibited this behavior (figure 4.4 (a), (b) and (c)).

The resulting cellular mode in a particular experiment with parameters in the region where coexistence of different modes is possible, was determined by the initial conditions and the path adopted in parameter space

to reach the experimental conditions. Consequently, mode switches could be induced by suitable perturbations such as noise, transient perturbations of the flow field or the fuel flow rate.

Close to extinction, a sequence of transitions could be induced between

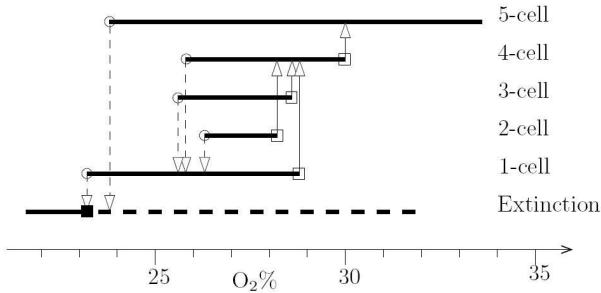


Figure 4.5: Reaction path of a cellular jet diffusion flame to changes in the co-flow composition. The jet has a hydrogen mole fraction of $X_{H_2} = 0.225$ and both streams are diluted with CO_2 . The jet and co-flow velocities are according to the experimental investigation of figure 4.3 [40]

the dominant five-cell state and the states with one to four cells. Figure 4.5 shows such a transition diagram between the states shown in figure 4.4 for the fixed fuel mole fraction of $X_{H_2} = 0.225$. The hysteretic transitions could either be observed by gradually changing the oxygen concentration or by inducing a large perturbation to the system. The transitions indicated by arrows in figure 4.5 are the forward (solid) and backwards (dashed) transitions observed experimentally during the gradual increase or decrease of the oxygen concentration.

The second study (study *B*) was performed with constant composition and velocity of the co-flow at $X_{O_2} = 1.0$ and $u_c = 4.66$ cm/s, while the velocity and composition of the jet was varied from $u_j = 37.7$ cm/s to $u_j = 339.5$ cm/s and $X_{H_2} = 0.15$ to $X_{H_2} = 0.21$, respectively [38]. Similar hysteretic behavior as in the first parameter study was observed. The resulting cellular modes for several jet flow velocities are summarized in Figure 4.6.

The detection of the number of cells was performed directly by visualization. In order to detect several cellular modes at one condition, the flame was manually disturbed using a bluff-body. The measurements were performed by fixing u_j and decreasing the concentration of hydro-

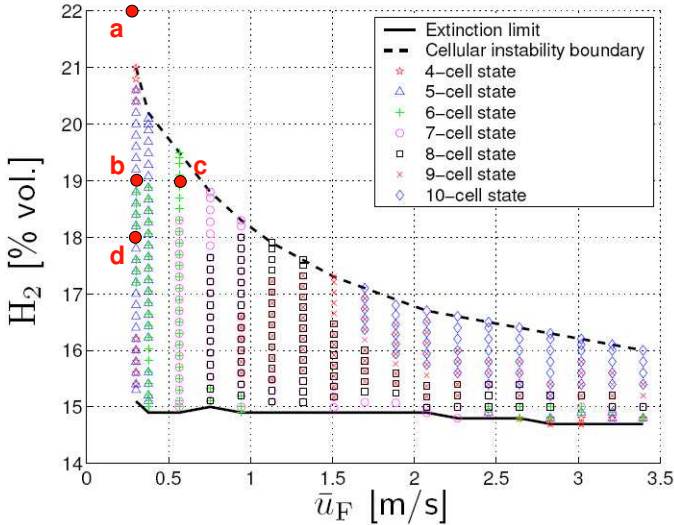


Figure 4.6: Extinction limit and boundaries of different cellular instabilities observed for CO_2 diluted H_2 jet with fixed velocity in a pure O_2 co-flow with $u_c = 4.66 \text{ cm/s}$. The centreline fuel velocity u_j and its composition are varied. [38]

gen. The extinction limit (solid line) could be determined exactly by reducing the hydrogen mole fraction in steps of 0.001. The upper cellular boundary (dashed line) was more difficult to define, since the cellular flames close to this line, are very close to each other, making the onset of different cellular states less clear. As it can be seen in figure 4.6, up to three different cellular modes were found to coexist for several conditions.

With increasing u_j , the number of cells increased and the limit for the appearance of cellular flames decreased. Since the extinction limit was found to be less sensitive to the jet velocity, the cellular zone became much smaller for higher jet velocities. For high jet velocities, cellular flames with large number of cells could be observed very near to the extinction limit.

The number of cellular flames in the jet diffusion flame was found to be related to the shear layer and therefore to the inlet velocity profile of the jet [39]. As scaling length for the shear layer, the vorticity thickness δ_ω

was used:

$$\frac{\delta_\omega}{d} = \frac{\bar{U}_{max} - \bar{U}_{min}}{\left| \frac{dU}{dr} \right|_{max}} , \quad (4.1)$$

where \bar{U} is the mean velocity and d the jet diameter. Since the co-flow velocity was low compared to the inner flow, the initial vorticity thickness was determined assuming $\bar{U}_{max} = u_j$ and $\bar{U}_{min} = 0$. The vorticity thickness was determined from the LDA measurements of the cold and the reacting jet, but the influence of the chemical reactions proved to be marginal very close to the nozzle. The vorticity thickness was shown to be proportional to the inverse square root of the Reynolds number ($Re_d = u_j d / \nu_F$, where ν_F is the viscosity of the fuel mixture).

$$\frac{\delta_\omega}{d} = 1.81 \frac{1}{\sqrt{Re_d}} \quad (4.2)$$

The integrated chemiluminescence images were analyzed with respect to the number of cells which are stabilized for the given boundary conditions. In order to define a wave number (λ), the diameter of the circle defined by the cellular flames (d_f) was determined from the chemiluminescence images. This diameter was found to be almost equal to the jet diameter for low velocities and decreased slightly for higher velocities. The wavelengths was then determined as follows:

$$\lambda = \frac{\pi d_f}{N_{cell}} , \quad (4.3)$$

where N_{cell} is the number of cells observed in the jet diffusion flame. This wave number related to the square root of the vorticity thickness including an empirical correlation of the initial mixture strength is plotted in figure 4.7 (The empirical coefficients are $\gamma = 0.22$ and $b = 2.83$ [38]). The circles represent the measurements for the axisymmetric burner considered here. For jet parameters, which have multiple stable cellular modes, it can be seen, that one stable solution is above and one below the line of the predicted relation. In the same plot, the same relation for a Wolfhard-Parker burner is given (squares), which is not considered in the presented work.

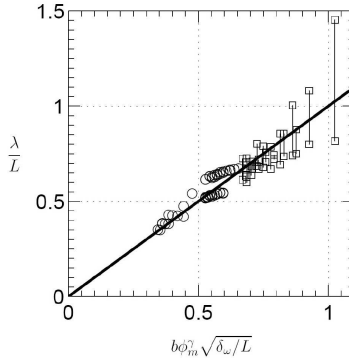


Figure 4.7: Relation of the measured vorticity thickness to the cellular wavelength for the axisymmetric jet (circles) and a Wolfhard-Parker burner (squares) from [38].

4.2 Computational set-up

The height and diameter of the cylindrical computational domain are each equal to six times the jet-diameter $d = 7.5 \text{ mm}$. Larger domains have been tested and the comparison of the results showed that the chosen size is sufficient and the domain boundaries have no influence on the flow field of the investigated flames. The velocity boundary conditions are Dirichlet at the inflow and zero-Neumann at the outflow. Since the co-flow region in the experiment has a diameter of ten times the nozzle diameter and is surrounded by free air, moving wall boundary conditions are applied at the cylinder shell. Temperature is fixed on the inflow and lateral boundaries to $T = 300\text{K}$, while flux boundary conditions are applied for the species on all boundaries.

The domain is discretized into 3168 spectral elements, within each of which 4th- or 6th-order interpolating polynomials are used. The computational mesh is displayed in figure 4.8. Other domain discretization have been tested with a focus on the accuracy of the results and the computational performance of the simulations. The number of spectral elements was varied from 468 to 5104 and the order of the polynomials was varied from 4th to 14th. For the results presented here, simulations with higher spatial resolution revealed no difference in the cellular structure of the flame, the liftoff height or the maximum temperature.

The detailed hydrogen mechanism of Li et al. [36] is employed, and

the chemical source term and transport properties are calculated with Chemkin II (see chapter 2). All computations were performed on a 64-CPU Linux cluster equipped with 2.0 GHz Intel Xeon processors.

The results presented here were all obtained without the effect of buoyancy, in order to reduce the computational cost of the simulations. The effect of buoyancy has been tested and it could be shown, that it influences the upper part of the flame, where a considerable acceleration of the burned gases can be observed. Its influence on the flame structure near the nozzle exit was found to be very weak, while the cellular mode of the flame was not affected at all. When buoyancy was considered, the acceleration of the flow in the upper part of the computational domain required a smaller integration time-step for the flow part and increased significantly the computational cost. This increased axial velocity was also associated with numerical problems at the outflow boundary due to negative axial velocities in the outer part of the domain occurring from a recirculation zone.

As Lo Jacono [38] observed, the cellular mode of the flame is related to the vorticity thickness of the jet. Consequently, the velocity inlet profile has a major impact on the resulting cellular mode. According to the design of the nozzle of the burner and measurements for higher jet velocities, a steep hyperbolic tangent top-hat profile was applied as inlet boundary condition for the simulations. Equation (4.4) gives the mathematical description of the axial profile (radial and azimuthal velocities are assumed

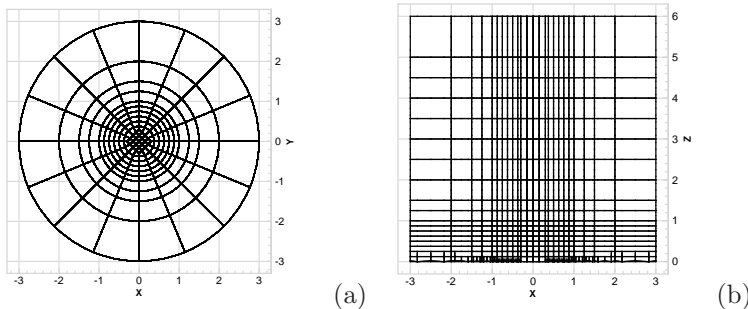


Figure 4.8: The computational domain with its 3168 spectral element skeleton in the (a) radial-azimuthal and (b) radial-axial directions.

to be zero):

$$w = u_c + \frac{u_j - u_c}{2} \left(1 - \tanh \left(\frac{r - (d/2 - \beta)}{\delta} \right) \right) \quad (4.4)$$

where w , δ and β are the velocity in the axial direction, a parameter to define the steepness of the profile and a correction value to shift the location of the point of $w = u_j/2$ towards the jet axis, respectively. Unless noted otherwise, the presented simulations were performed with inlet velocity profiles defined with $\delta = 0.05$ and $\beta = 0$, scaled only by u_j and u_c . Similar, but steeper profiles ($\delta = 0.01$) were assumed for the species flux boundary conditions (the exact physical processes at the rim of the nozzle are not known). The applied axial profiles for velocity and species are plotted in figure 4.9.

The initial condition for the simulations was also important, as it could influence the resulting flame structure due to the existence of multiple steady states for the same conditions. For the presented problem, the initial condition must be a burning one, otherwise the cold gases would have to be ignited applying a hot-spot in the domain. The ignition of the flame initialized by a hot-spot would be a delicate phase to simulate,

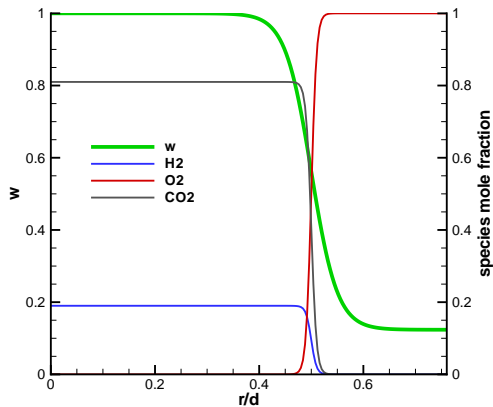


Figure 4.9: Normalized inflow profile of velocity (green) and the inflowing species.

numerically and computationally. For the presented simulations, a fully burning, axial symmetric flame was used as initial condition, which was obtained in a two-dimensional axisymmetric domain. The jet was ignited by applying a hot-spot in the shear layer. The fast two-dimensional simulation result was rotated around the axis of symmetry in order to generate a three-dimensional initial condition.

The two experimentally investigated cases (*A* and *B*) were also considered for the numerical studies. In the parametric study *A*, the jet and co-flow velocities were fixed to $u_j = 76 \text{ cm/s}$ and $u_c = 4 \text{ cm/s}$ and the fuel and oxidizer mole fractions of the CO_2 -diluted jet and co-flow were fixed to $X_{H_2} = 0.225$ and $X_{O_2} = 0.275$, respectively.

In case *B*, the co-flow consisted of pure oxygen and its velocity was fixed to $u_c = 4.66 \text{ cm/s}$, whereas the jet velocity was varied from $u_j = 37.7 \text{ cm/s}$ to $u_j = 94.3 \text{ cm/s}$ and the hydrogen mole fraction in the fuel jet in the range from $X_{H_2} = 0.18$ to 0.22 .

Many difficulties were encountered while trying to obtain numerical results of the above discussed flames. Since transient effects are of importance, a transient code was applied. This enabled to investigate the formation of the cellular structures as well as the change from one solution to another. The time for a cellular mode to form and to obtain its steady-state according to a new boundary condition, is very large compared to the numerically applicable simulation time step. The required computational time is always a critical issue in three dimensional DNS, but is even more severe due to the slow formation of the desired flames. An additional difficulty associated with the simulation of these weakly burning flames is flame extinction, which is a valid and obviously stable solution, but not the desired one.

The response of the flame to a change in boundary conditions, where the existing cellular mode was not the favorable, was always a reduction of the maximum temperature and a slow increase of the lift-off height of the flame. From this point on, the flame undergoes transition to a number of non-symmetric states and eventually reaches a stable one, which, if the lift-off height is not already too large, leads to intensified combustion and movement of the flame towards the jet nozzle. If no stable mode is reached, or the flame is too far from the nozzle, the flame propagates slowly away from the nozzle and eventually extinguishes. Unfortunately, in most cases the change of conditions resulted in the extinguished solution.

The main problem in the simulation of such flames is that it is computationally expensive to simulate the flame until the point, where it becomes clear that the flame will undergo a transition to another stable flame

mode or whether the flame extinguishes.

The same behavior was observed experimentally, where the flame extinguishes often in response to a change in the boundary conditions when it was not stabilized by a bluff-body. During extinction, in the experiment as well as in simulations, the flame is lifted further away from the nozzle and a transition through a number of cellular states can be observed.

If the boundary conditions is changed in a way, that the current solution is not sustained anymore, the time for a new cellular mode to be stabilized is around 200 *ms*, while flame blow off could be safely concluded after ~ 100 *ms*. The integration time-step for the presented simulations was 0.002 *ms*. Therefore the transient simulation of a change in the cellular structure of the flame due to a change in boundary conditions required around 100'000 time-steps. Most of the simulations were performed on 16 CPUs of a Linux cluster where the simulation of 1 *ms* of real time required approximately ten hours.

4.3 Comparison with the experiments

4.3.1 Case A: Variation of jet and co-flow composition

The first simulations of the cellular flames were performed on the basis of the results of LoJacono et al.[40] summarized in figure 4.3. The most interesting configuration of this study is the one with a fuel composition of $X_{H_2} = 0.225$ and a co-flow composition of $X_{O_2} = 0.275$, since for this configuration, all five cellular modes presented in figure 4.4 were observed experimentally. The same fuel concentration was also used for the definition of stability boundaries of the different cellular modes summarized in figure 4.5.

The computed result was a five-cell state shown in figure 4.10 in terms of iso-contour plots of temperature, water and *OH* mass fractions, on a plane 0.5 *d* above the nozzle. The cells form a circle with radius larger than the nozzle (the nozzle is indicated with a black circle), which is due to the fast diffusion of the hydrogen. As expected, the water mass fraction distribution shows the same characteristic as the temperature field. The *OH* mass fraction distribution, consisting of long and narrow cells, is a good indication for the location of the reaction zone. The size of the cells varies slightly, but no further analysis of this phenomenon was performed. The corresponding experimental result (figure 4.4 (e)), shows also a not completely symmetric cell distribution and cells which are not of equal size. There is no correlation of the distributions of the cells and

the symmetry of the grid employed in the simulations.

The formation of a five-cell state is in agreement with the experimental findings, where for the conditions considered only a five-cell state was stabilized spontaneously [38]. Transition to one of the other four stable cellular modes for the given conditions (figure 4.5) could only be realized by inducing a mechanical disturbance to the flame.

In order to be able to map figure 4.5 with simulations, a variation of the co-flow composition would be required. Such a variation was done experimentally in order to evaluate the stability boundaries of the cellular modes (figure 4.5). Due to the low co-flow velocity (compared to the jet velocity), a change in the co-flow composition would take long time to propagate through the computational domain. The required computational time for the transient simulation of a new co-flow composition filling the whole computational domain would be too long for the available resources. The propagation of a new co-flow composition is also hindered

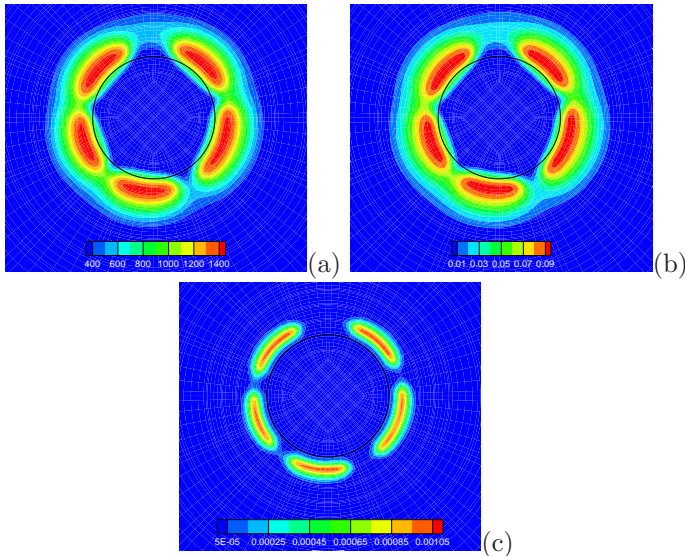


Figure 4.10: Simulated iso-contour plots on a plane $0.5 d$ above the nozzle for (a) temperature, (b) H_2O and (c) OH of the five-cell flame for $u_j = 76$ cm/s and $u_c = 4$ cm/s . The CO_2 diluted streams have mole fraction of $X_{H_2} = 0.225$ in the jet and $X_{O_2} = 0.275$ in the co-flow.

by the entrainment of the jet from the outer part of the co-flow and the associated reduction in co-flow velocity due to a weak recirculation zone. The only parameters which can efficiently be varied in the simulations are the hydrogen concentration in the jet and the jet velocity. However, in the region of the considered oxygen mole fraction of $X_{O_2} = 0.275$, the simulated five-cell mode is dominant and the flame mode could not be changed by any change in the hydrogen concentration in the experiment. A change from the five-cell mode to one of the other reported modes could only be archived by mechanical disturbance of the flame. A variation of the jet velocity was not of interest here, because no experimental data are available for the investigated conditions.

4.3.2 Case B: Variation of the jet composition and velocity

In this study, Lo Jacono [38] varied two parameters, which can effectively be varied in simulations: The composition and velocity of the jet stream. The co-flow composition and velocity remained unchanged. Compared to case *A*, where also the composition of the co-flow was varied, a change of the inflow conditions of the fast flowing jet propagates much faster through the domain. The other important aspect of this study is, that it suggests, that a change in the cellular mode can be affected by changing the fuel-composition or the jet-velocity, at least for some well-chosen combinations of jet velocity and composition. For the obtained five-cell state in case *A*, only mechanical perturbation provoked a change of the cellular mode in experiment. The experimental results are summarized in figure 4.6.

The first condition, which was numerically investigated was the one of a fully-burning flame for the conditions of point *a* in figure 4.6. As in the experiment, a strongly-burning axisymmetric flame with a maximum temperature of 1596 K was obtained. The simulation result is presented in figure 4.11, where temperature iso-contours on a vertical plane through the jet axis (4.11 (a)) and on a horizontal plane $0.5\ d$ above the nozzle are plotted. As it can be clearly seen, the flame is practically attached to the nozzle. The hot gases convect and diffuse through the domain, where they are cooled down by mixing with the surrounding oxidizer. Due to the fast radial diffusion of the hydrogen, the flame (high temperature zone of $> 1300\text{ K}$) is almost straight instead of bending towards the jet axis, as expected for over-ventilated flames (see chapter 1). A zone of lower temperature “closes” the flame around $1.5\ d$ above the nozzle. Figure

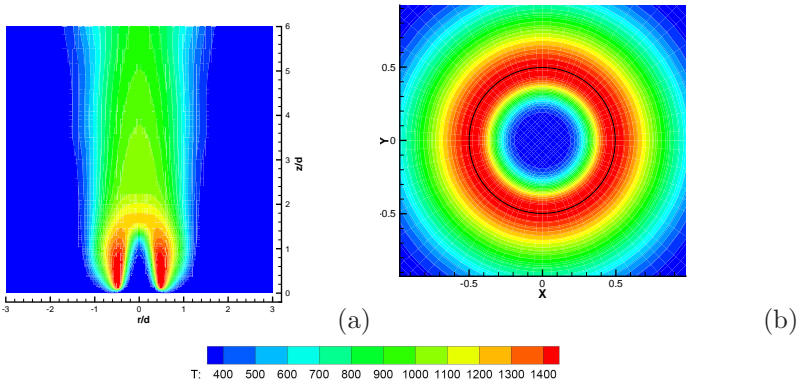


Figure 4.11: Temperature contour plot on (a) a vertical plane through the jet axis, and (b) on a horizontal plane $0.5 d$ above the nozzle for parameters as in point *a* of figure 4.6 (Jet: $u_j = 37.7 \text{ cm/s}$, $X_{H_2} = 0.21$; co-flow: $u_c = 4.66$, $X_{O_2} = 1.0$)

4.11 (b) shows iso-contours on a horizontal plane through the flame. The flame is contiguous without any sign of cellular instabilities as observed in the experiments.

Starting from the state of figure 4.11, the hydrogen mole fraction in the jet was decreased from $X_{H_2} = 0.21$ to $X_{H_2} = 0.19$ (figure 4.6, $a \rightarrow b$). The transition from the strongly-burning attached flame to an eight-cell lifted flame is presented in the sequence of figure 4.12. Showing temperature iso-contours on a plane $0.5 d$ above the nozzle: The flame first splits into four cells which then further subdivide until a stable eight-cell state is obtained. Simulations with higher resolution gave the same result and confirmed that the resulting eight-cell state does not depend on the symmetry of the computational mesh. The formation of cellular flames in response to the decrease in fuel concentration is in agreement with the experimental findings, but the resulting cellular mode could not be observed experimentally for the given conditions; this issue will be discussed later on.

The overall change of the fully burning flame of figure 4.11 to the eight-cell state presented in figure 4.12 is also a change from a strongly burning flame which is almost attached to the nozzle, to a flame with a lift-off height equal to $0.45 d$. This large distance of the flame to the nozzle

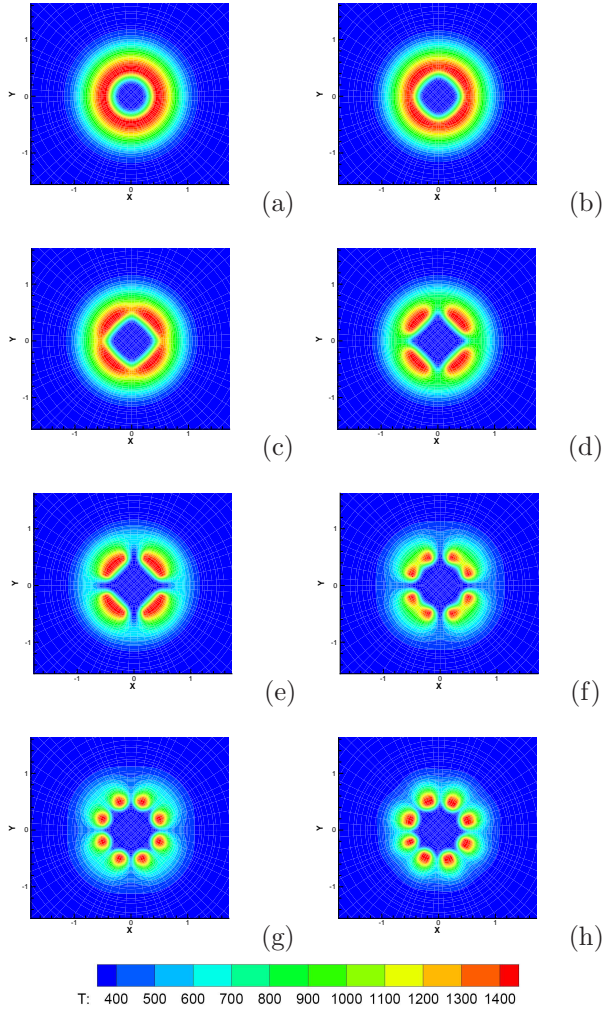


Figure 4.12: Temperature iso-contours on a plane $0.5 d$ above the nozzle. The axisymmetric flame undergoes a transition to an 8-cell state due to the reduction of H_2 mole fraction from $X_{H_2} = 0.22$ to $X_{H_2} = 0.19$. The velocities of jet and co-flow are $u_j = 37.7 \text{ cm/s}$ and $u_c = 4.66$, respectively. The time sequence is at $t=31.8, 37.8, 45.8, 63.7, 89.5, 97.5$ and 119.2 ms for images (b)-(h), respectively. (Jet: $u_j = 37.7 \text{ cm/s}$; co-flow: $u_c = 4.66$, $X_{O_2} = 1.0$)

changes the characteristic of the flame, because fuel and oxidizer can now be mixed in the shear layer prior to combustion and the diffusion flame of the fully burning flame becomes to a partially premixed one. Parts of the flame have strong premixed flame characteristics as on the lowest edge of the flame, where partially premixed gases are convected towards a stationary flame front. On the other hand, looking at one of the cellular flames in the radial direction, the flame is clearly diffusion-controlled with fuel on one side of the flame and oxidizer on the other. The issue of partial premixing is discussed in more detail below. Figure 4.13 compares the lift-off height of the burning flame with the one of the weakly-burning flame in the eight-cell mode.

The mixture fraction (ξ_{st}) is defined according to [27, 47] as follows:

$$\xi = \frac{0.5Z_H/W_H + (Z_{O,Ox} - Z_O)/W_O}{0.5Z_{H,F}/W_H + Z_{O,Ox}/W_O} \quad (4.5)$$

where W_H and W_O are the atomic weights of hydrogen and oxygen, respectively. $Z_{O,Ox}$ and $Z_{H,F}$ are evaluated according to [47] and represent the mass fraction of oxygen in the oxidizer stream and hydrogen in the fuel stream, respectively. The stoichiometric mixture fraction for the fuel and oxidizer used in this study is $\xi_{st} = 0.922$. For the lifted flame (figure 4.13 (b)) the stoichiometric mixture fraction is indicated with a black line.

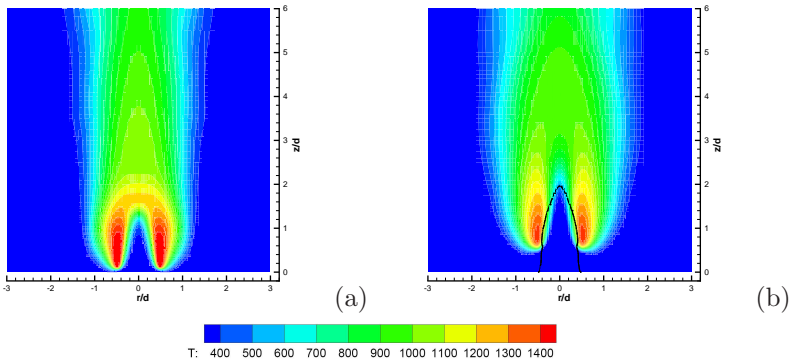


Figure 4.13: Temperature contour plot on a vertical plane through the jet axis for the flames with $X_{H_2} = 0.22$ (a) and $X_{H_2} = 0.19$ (b). The velocities of jet and co-flow are $u_j = 37.7$ cm/s and $u_c = 4.66$, respectively.

As further simulations and the experimental investigations show, the

number of cells depends on the velocity profile of the jet at the nozzle exit. The steepness of the jet velocity profile is a parameter which can only be varied by changing the Reynolds number in the experiment, but which can be easily specified in the simulations.

The lack of detailed measured results of the velocity profiles for the given conditions was the reason for the use of axial velocity profiles adapted from available measured jet velocity profiles for higher velocities (equation (4.4) with $\delta = 0.05$). LDA measurements of jet inlet velocity profiles similar to those considered here, which were performed after the simulations presented in figure 4.12 were performed, showed smoother velocity profiles than were assumed for the simulations. Even though, the velocity profile was measured for a slightly higher inlet velocity ($u_j = 65.0 \text{ cm/s}$), the normalized profile can be assumed to be similar for the considered velocity of $u_j = 37.7 \text{ cm/s}$. For the following simulations, the inlet velocity profile was adjusted to the new experimental data. The old jet velocity profile ($\delta = 0.05$ and $\beta = 0.0$), the new, smooth profile ($\delta = 0.099$ and $\beta = 0.084$) and the experimental measured profile are plotted in figure 4.14. The smoother profile is applied in all the simulations presented below. The influence of the new velocity boundary condition is shown for a simulation where the initial condition is the eight-cell results presented in figure 4.12 and only the velocity profile was changed. The transient results of the simulation performed with the new velocity profile with $\delta = 0.099$ and $\beta = 0.084$ is shown in figure 4.15. The final five-cell state is in agreement with the experimental finding (figure 4.6, point *b*). During the transient from the eight to the five-cell state, three cells extinguished and the remaining five cells enlarged in azimuthal direction and rearranged almost symmetrically.

As mentioned in section 4.1.1, the experimental data consist only of axially integrated passive chemiluminescence images and some velocity field measurements (LDA) of the jet velocity profiles. The comparison with simulation results is not straightforward, because of two reasons: First, the passive chemiluminescence captures only the excited molecules which emit light, while the simulations provide the concentration of species in the ground state. Second, the axial integration does not capture important information as lift-off height and length of the flame. Therefore, a comparison of experimental and numerical results can only be done by evaluating the cellular mode of the flame and no other quantitative comparison is possible.

The chemiluminescence images from the experiment show mainly the light emitted by the excited *OH* radical. For the comparison presented in

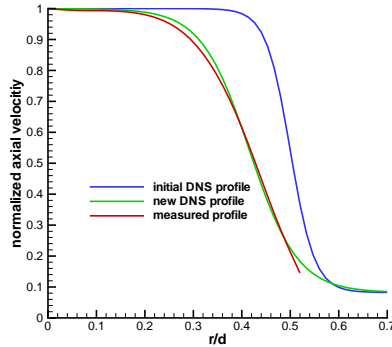


Figure 4.14: Normalized (blue) initial inflow profile ($\delta = 0.05$ and $\beta = 0.0$) compared to (red) the experimental LDA conditions and (green) the new velocity profile for the simulation ($\delta = 0.099$ and $\beta = 0.084$).

figure 4.16, the computed values of the OH -mass fraction in the computational domain were integrated along the axial direction of the jet. The experimental and numerical results thus obtained are in good qualitative agreement (figure 4.16).

Figure 4.17 shows iso-contours of some of the species mass fractions on a horizontal plane $0.5 d$ above the nozzle. The iso-contour plot of the hydrogen concentration (figure 4.17(a)) shows clearly the five cells in the regions where all the fuel is consumed. Between the cells as well as in the lift-off distance of the flame, the fuel diffuses into the co-flowing oxidizer stream, resulting in a certain degree of premixing of fuel and oxidizer. Therefore, the flame is no longer a pure diffusion flame, as was the case for the anchored flame. This premixing results in the non-zero concentration of fuel on the oxidizer side of the flame. Nevertheless, the location of the maximum concentration of the hydrogen radical (figure 4.17(c)) shows a strong diffusion flame character. The maximum hydrogen radical concentration is closer to the high hydrogen concentration in the center of the jet. The OH concentration plotted in figure 4.17(d) is a good indication for the location of the flame, which is slightly within the circle marking the nozzle. Figure 4.17(b) shows the water concentration, which is high in the burning cells and extends towards the co-flow region. This is because of the low velocity of the co-flow, which does not carry away the combustion

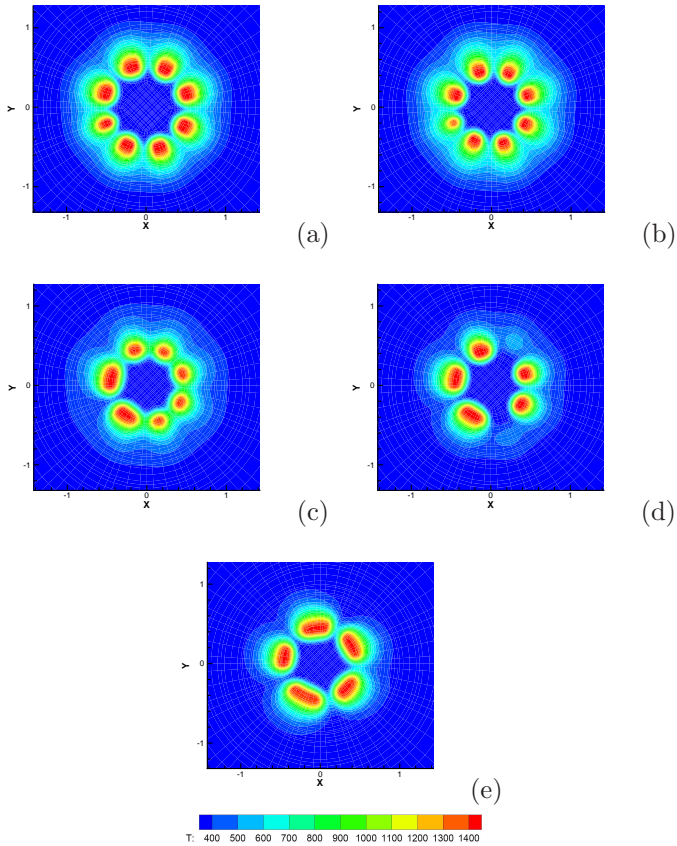


Figure 4.15: Temperature contour plots on a horizontal plane $0.5 d$ above the nozzle. The flame undergoes a transition from the 8-cell to the 5-cell flame after a modification of the inflow velocity profile to match the vorticity thickness of the inlet plane velocity profile. The time sequence is at $t=13.9, 25.9, 37.8$ and 79.6 ms for images (b)-(e), respectively. (Jet: $u_j = 37.7$ cm/s, $X_{H_2} = 0.19$; co-flow: $u_c = 4.66$, $X_{O_2} = 1.0$)

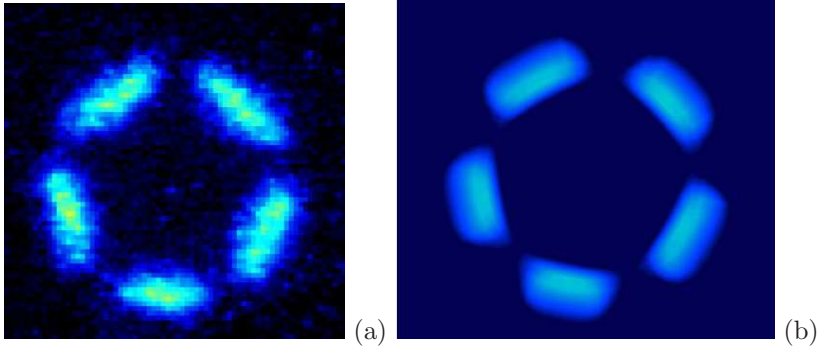


Figure 4.16: Passive (integral) chemiluminescence picture from (a) the experiment compared with (b) an integrated OH mass fraction result from the simulations. (Jet: $u_j = 37.7 \text{ cm/s}$, $X_{H_2} = 0.19$; co-flow: $u_c = 4.66$, $X_{O_2} = 1.0$)

product as fast as it is convected away in the jet. Figure 4.17(e) shows a three-dimensional iso-surface of the OH mass fraction ($Y_{OH} = 4.25 \cdot 10^{-4}$). The cellular flames have a broad lower base and become narrow towards the top. The wide flame is due to the partial premixing in the lower part of the cell. For the given low reactivity, premixing results in a wide flame and not in a triple flame structure as it would form in a flame with higher reactivity. In the upper, mainly diffusive part, combustion takes place in a narrow region. The structure of the flame is discussed in more detail below.

Besides velocity, temperature and species fields, other interesting information can be obtained from the simulations. Some of them are presented in figure 4.18, where the mixture fraction, the normalized heat release rate and the production terms of OH and H and the flame index (FI) are plotted.

In figure 4.18 (a), the mixture fraction is plotted with the stoichiometric mixture fraction indicated with the dashed circle. It can be seen, that intense combustion takes place in lean conditions. This is due to the oxygen mole fraction of $X_{O_2} = 1$ in the co-flow which enables the flame to stabilize in much leaner conditions, than it is possible in flames, where air is used as oxidant. The second reason is, that in the lean region, where the flame is stabilized, the jet-velocity is significantly lower, than closer to the center of the jet where the flame would be carried away by the jet. The

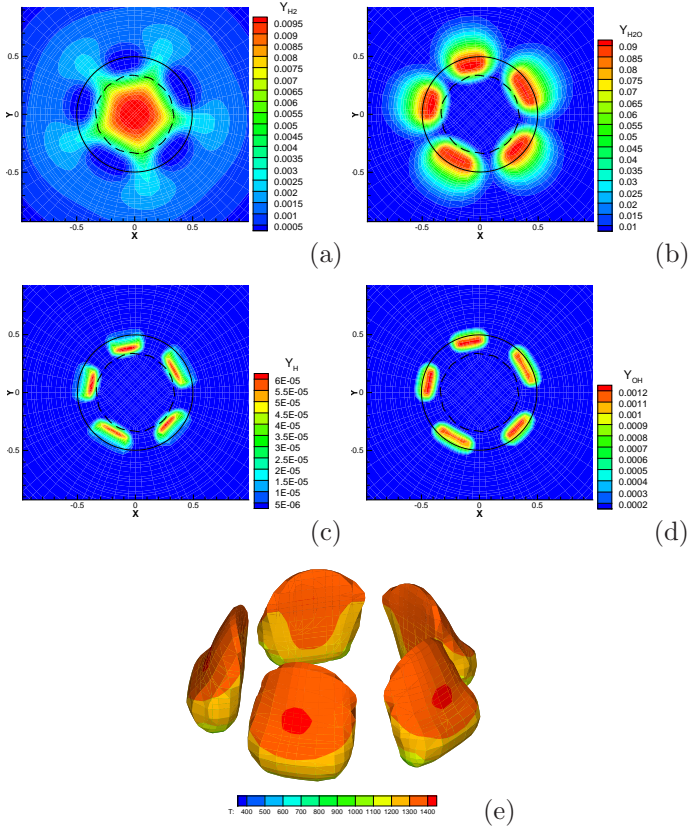


Figure 4.17: Species mass fraction on a plane $0.5 d$ above the nozzle for (a) H_2 , (b) H_2O , (c) H and (d) OH and (e) a three-dimensional iso-surface OH plot ($Y_{OH} = 4.25 \cdot 10^{-4}$) of the 5-cell state of point B in figure 4.6 colored with temperature. The dashed line represents ξ_{st} . (Jet: $u_j = 37.7$ cm/s, $X_{H_2} = 0.19$; co-flow: $u_c = 4.66$, $X_{O_2} = 1.0$)

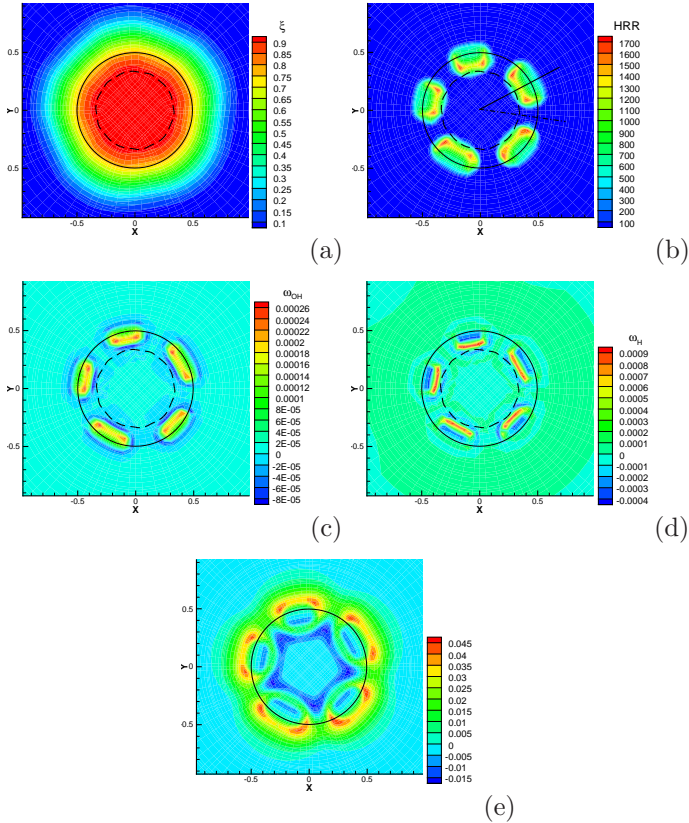


Figure 4.18: (a) Mixture fraction (with stoichiometric mixture fraction indicated with the dashed circle), (b) normalized heat release rate, (c) OH and (d) H source term and (e) the flame index ($FI = \nabla Y_{H_2} \cdot \nabla Y_{O_2}$) on a plane $0.5 d$ above the nozzle of the 5-cell flame. (Jet: $u_j = 37.7$ cm/s, $X_{H_2} = 0.19$; co-flow: $u_c = 4.66$, $X_{O_2} = 1.0$)

axially asymmetric shape of the mixture fraction distribution is due to the fast hydrogen diffusion into the cellular flames. In figure 4.18 (b) the heat release rate is plotted. An increased heat release in the convex part of the flames towards the limiting reactant can be observed. The convex curved part of the cell increases the area between the hot flame and the cold jet containing the limiting reactant (hydrogen). In the present low Lewis number flame, heat diffusion is slower compared to the diffusion of the limiting reactant. Therefore the increased area between the hot reaction zone and the cold hydrogen jet leads to slightly increased heat loss but strongly increased availability of fuel in the reaction zone. This results in higher temperature in this curved part of the flame.

The production rate of OH is plotted in figure 4.18 (c). The hydroxyl radical is produced in the flame and consumed on the oxidizer as well as on the fuel side. At this height, much more of the species is produced than consumed, most of the species is convected with the jet and consumed higher up in the flame. The chemical source term for the hydrogen radical (d) shows two distinct zones, the one close to the center of the fuel jet, where the radicals are produced and the one closer to the co-flow, where the radicals are consumed.

The flame index ($FI = \nabla Y_{H_2} \cdot \nabla Y_{O_2}$) plotted in figure 4.18 (e) indicates whether the flame is dominated by the diffusive or the premixed character [55, 16]. Positive values of this term indicate that in the dominant diffusion direction fuel and oxidizer diffuse from the same side into the reaction zone, which is typical for a premixed flame. Negative values of FI , as they can be seen at the inner part of the flames, indicate diffusion-dominated combustion. The positive values on the outer part of the flames and especially at the flame edges, indicate premixed combustion. The strongly positive edges indicate the premixing in the non burning part between the cellular flames. This term is analyzed in more detail in figure 4.21.

The velocity, temperature and species mass fraction profiles in the radial direction $0.5 d$ above the nozzle are plotted in figure 4.19. The first two plots show the profiles on a line (figure 4.18 (b) solid line) from the center through a burning cell (figure 4.19 (a), (b)) of the five-cell flame. In this plot the peak in the combustion zone can be clearly seen for temperature, OH and water vapor. Comparing the oxygen concentration to the cold flow concentration, a strong influence of the flame can be observed. As the comparison with the concentration in the non burning part (figure 4.19 (c)) shows, are the species mass fraction influenced by the modified velocity field due to combustion. In the combustion zone, the oxygen concentration is reduced to a mass fraction of $Y_{O_2} = 0.025$ and stays al-

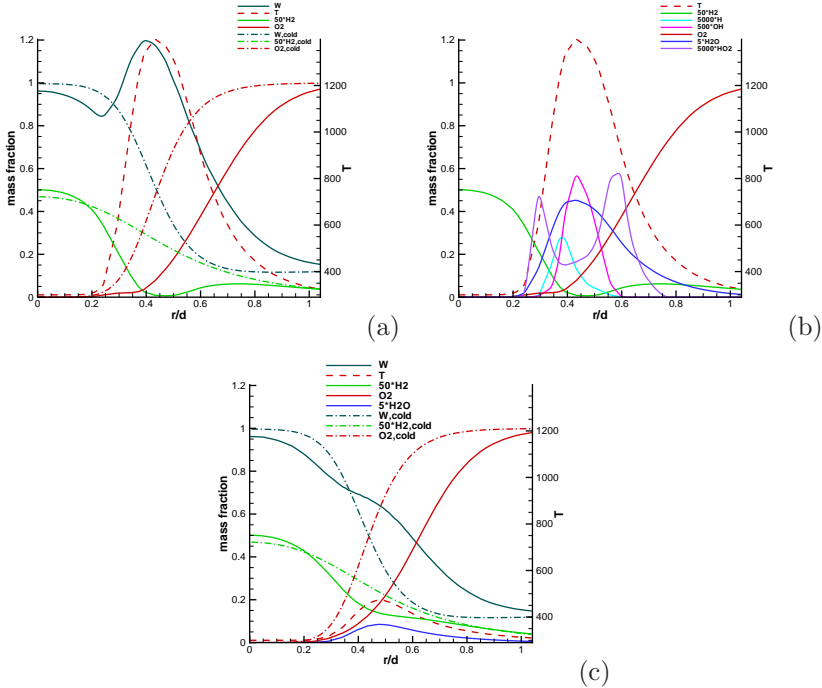


Figure 4.19: Normalized temperature, velocity and species mass fraction profiles on a plane $0.5 d$ above the nozzle along a line starting from the center and cutting through (a) and (b) a cell of the 5-cell flame, (c) through the non-burning part. The dash-dotted lines are the cold-flow (pure mixing) results. (Jet: $u_j = 37.7 \text{ cm/s}$, $X_{H_2} = 0.19$; co-flow: $u_c = 4.66$, $X_{O_2} = 1.0$)

most constant for $0.25 < r/d < 0.35$, in the rich part of the flame. This is an indication, that in this region, due to the strong dilution and the low temperatures, oxygen can not be fully consumed. The HO_2 radical is formed prior to the strongly reacting zone, in regimes of relatively low temperature where H -radicals and oxygen coexist. At higher temperatures, HO_2 is converted into OH . Due to premixing, the mass fraction of HO_2 shows two peaks, one on the fuel and one on the oxidizer side of the flame. The distribution of hydrogen shows full consumption in the flame region, where its mass fraction is very close to zero. The hydrogen mass fraction on the oxidizer side is up to 10 % of the maximum hydrogen

concentration, which is mainly due to the premixing of the gases caused by the large lift-off height of the flame. Additionally, the hydrogen concentration on the oxidizer side is increased by hydrogen diffusion through the non-burning zones between the cellular flames.

The profiles through the non-burning part of the flame (figure 4.18 (b) dash dotted line) in figure 4.19 (c) are influenced by the flame as well, but especially the hydrogen species profile is close to the non-reacting state. Only near to the flame, its concentration is reduced due to diffusion in the azimuthal direction into the flame region. As in the cold flow result, the strongly diffusing fuel penetrates far into the co-flow region. The temperature is increased due to heat transfer from the burning zone into the non-reacting part. The gas expansion due to this increased temperature is, together with the viscous effects, responsible for the velocity increase between the burning zones compared to the cold flow. The non-zero water vapor concentration is due to diffusion in the azimuthal direction of the combustion product.

Figure 4.19 shows the partially premixed character of the flame. The profiles of fuel and oxidizer are close to the theoretical profiles for a perfect diffusion flame (reduction to zero in the reaction zone), but especially the non-zero fuel concentration on the oxidizer side results from premixing. This premixing, with the associated two peaks of the HO_2 concentration, will be analyzed in more detail below.

In the energy and species equations, the terms for convection, diffusion and chemical reaction balance each other for the steady five-cell state described above. The profiles of the different terms are plotted in figure 4.20 for energy, hydrogen and oxygen along lines from the jet axis in the radial direction (figure 4.18 (b) solid line) at the flame base ($z = 0.4375 d$), through the strongly burning part ($z = 0.5 d$) and above the zone of strongest reaction ($z = 0.5625 d$). The convection term is dominated by the axial component, while the velocities in the radial and azimuthal directions are very small. The diffusion term is dominated by the radial term except at the lowest tip of the flame, where large gradients in the axial direction result in large axial diffusion terms.

At the flame base (figure 4.20 (a)-(c)), one can see for the energy equation (figure 4.20 (a)), that the heat diffusion (black) and convection (blue) almost balance each other, as if a premixed flame front is stabilized in a flow. The reaction zone (red) is narrow and the reaction intensity low. The hydrogen species concentration is also dominated by the diffusion and the convection term (figure 4.20 (b)). Very close to the flame, similar to a premixed flame front, axial diffusion plays an important role and the

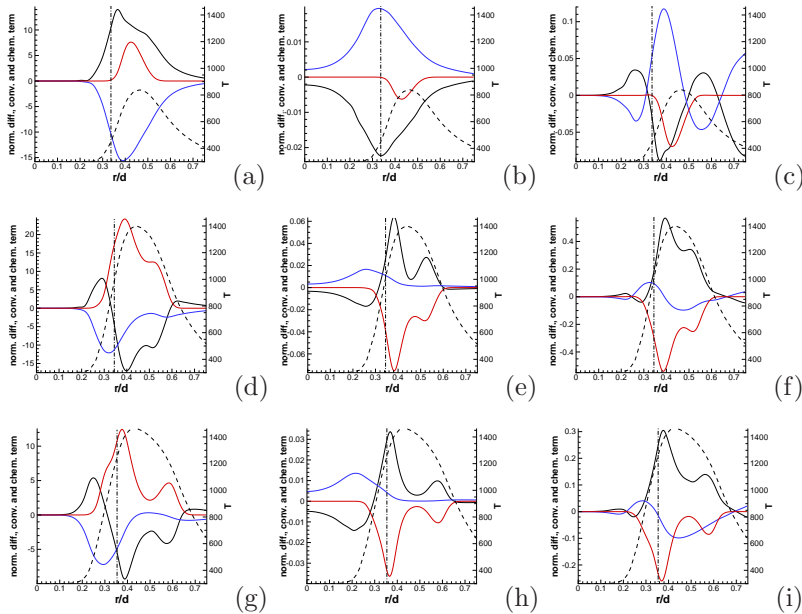


Figure 4.20: The balance of terms in the radial direction from the jet center through a cellular flame. Plotted are the diffusion (black), the convection (blue) and the reaction term (red) of the energy equation ((a),(d),(g)), the hydrogen ((b),(e),(h)) and oxygen ((c),(f),(i)) equations at $z = 0.4375 d$ (a-c), $z = 0.5 d$ (d-f) and $z = 0.5625 d$ (g-h). The temperature is plotted (dashed line) to indicate the location of the flame. The location of ξ_{st} is marked by the dash-dotted line. (Jet: $u_j = 37.7 \text{ cm/s}$, $X_{H_2} = 0.19$; co-flow: $u_c = 4.66$, $X_{O_2} = 1.0$)

negative diffusion term is influenced by that. Similar observations can be made about the oxygen terms (figure 4.20 (c)). The convection term is large, since fresh mixture is convected from below. The diffusion term is influenced by the large gradients in the flame and oxygen diffuses in the axial direction. The similar location of the minima of the diffusion terms of hydrogen and oxygen indicate the premixed character of the flame at its lowest tip.

At $z = 0.5 d$, two reaction zones can be distinguished: One (strong) towards the fuel and the other (weak) towards oxygen. The diffusion

term is again dominated by the radial component. In the energy equation (figure 4.20 (d)), the diffusion and the convection terms are balanced in the region just before the flame ($0.2 < r/d < 0.3$) where the heat is conducted from the hot reaction region towards the cold fuel jet and preheats the fuel. The heat is convected away, mainly in the axial direction, due to the dominant axial velocity component. In the burning region ($0.35 < r/d < 0.6$) convection is small and the diffusion term balances the reaction term. The diffusion term has two maxima at the inner and outer side of the flame due to the large temperature gradient towards the cold jet and oxidizer streams. The reaction is more intense close to the fuel side, since hydrogen is the limiting reactant for the conditions considered here.

The balance of terms in the hydrogen conservation equation (figure 4.20 (e)) can also be separated into a zone prior to the flame ($0.0 < r/d < 0.3$), where hydrogen diffuses in the radial direction towards the reaction zone. This diffusive flux is compensated by the axial convection of the fuel from the jet nozzle. In the reaction zone ($0.35 < r/d < 0.6$), the diffusion term is balanced by the reaction term, because all the hydrogen diffusing into the reaction zone is consumed in the flame. The two local maxima of the diffusion term indicate two zones with intensified combustion. In addition to the expected first zone, where most of the fuel is consumed, the second zone exists partially due to diffusion of fuel from the oxidizer side into the reaction zone. This is possible due to the above discussed (figure 4.19) premixing in the shear layer prior to the flame and between the flame cells. Further investigations on the two reaction peaks are presented below.

For oxygen (figure 4.20 (f)), non-zero convective fluxes before the flame ($0.25 < r/d < 0.4$) indicate the premixing in the shear layer prior to the flame. The oxygen which is mainly convected in the axial direction diffuses mainly in the radial direction into the reaction zone and is consumed by the chemical reactions. The diffusion is mainly towards the jet axis. The major part of the oxygen taking part in combustion diffuses from the co-flow region into the flame. The shape of the reaction term profile is almost equal to the one of the hydrogen also showing two zones of increased reactivity.

Further up in the flame, at $z = 0.5625$ (figure 4.20 (g)-(i)), the reaction intensity is much lower compared to the one at $z = 0.5 d$. The pronounced two reaction peaks can still be seen. Their distance increased due to the wider flame, and the outer peak became smaller.

In an attempt to distinguish premixed and diffusion dominated parts

of the flame, the FI plotted in figure 4.18 (e) is analyzed in the radial direction for the three heights considered above. In figure 4.21, the values for the three heights are plotted together with the associated temperature and the value for the hydrogen chemical reaction term for easy comparison to figure 4.20. Negative values of the flame index in the

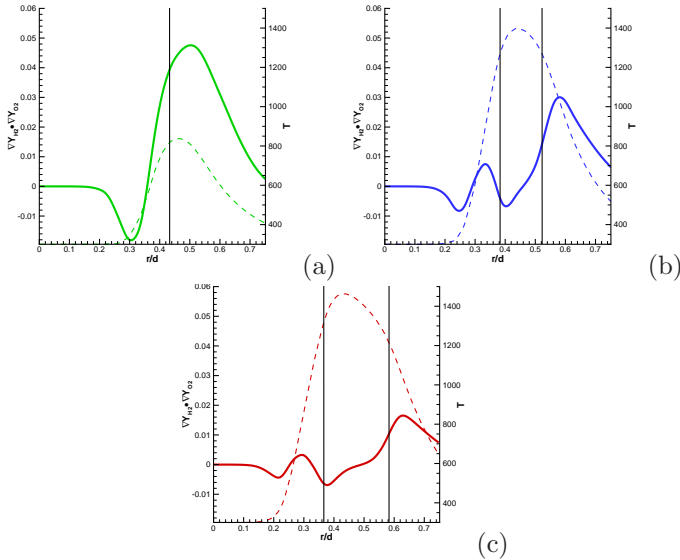


Figure 4.21: Flame index (solid line) and temperature (dashed line) at (a) $z = 0.4375 d$, (b) $z = 0.5 d$ and (c) $z = 0.5625 d$. The black vertical lines indicate the local minima of the hydrogen production terms (maximum reaction intensity, values see figure 4.20).

reaction zone indicate diffusion controlled flames, while positive values indicate that oxidizer and fuel approach from the same direction and the flame has therefore premixed character. In the present partially premixed flame, no distinct separation of the flame is possible, but dominant effects for the reaction peaks can still be discerned.

At the lowest height (green curve), the weak reaction peak correlates with a very large positive value of the flame index and has therefore strong premixed character. This finding is consistent with the previously discussed observations. At $z = 0.5 d$ (blue curve), the strong reaction peak close to the jet axis appears at a slightly negative flame index indicating that diffusion is the driving mechanism in the flame. The

second, less intense peak in the reaction intensity correlates with clearly positive values of the flame index and is therefore dominated by premixed combustion. Similar observations can be made for the investigation further up in the flame. The strongly burning zone closer to the jet is mainly diffusion controlled and the weaker reaction zone in the outer part of the flame has a strong premixed character.

In an attempt to capture the experimental observations of figure 4.6, simulation of cellular modes for flames with higher jet velocities or lower fuel concentration were performed. Unfortunately, due to the very sensitive dependence of the flames to the operating conditions (also observed experimentally), only few stable cellular modes could be obtained numerically. In all other cases, the flame slowly lifted off the nozzle and eventually blew off. One of the “successful” simulations resulted in the seven-cell state for the conditions of point *c* in figure 4.6 with $u_j = 56.6$ *cm/s* (fuel and oxidizer compositions were kept unchanged at $X_{H_2} = 0.19$, $u_c = 4.66$, $X_{O_2} = 1.0$). The increase in the jet velocity results in a reduction of the vorticity thickness at the location of the flame and therefore, according to [38], to an increase in the number of cells. The seven-cell mode was not reported experimentally, but it was observed for slightly lower fuel concentration in the jet.

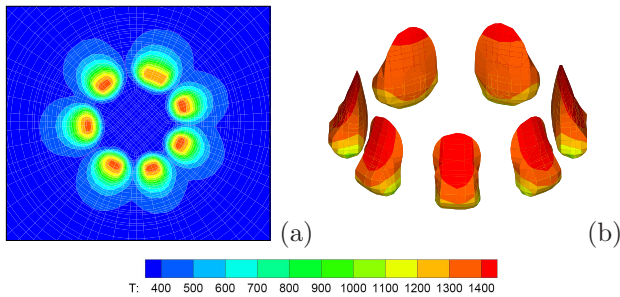


Figure 4.22: (a) Iso-temperature contours on a plane $0.5 d$ above the nozzle; (b) $Y_{OH} = 7.0 \cdot 10^{-4}$ iso-surface of a seven-cell flame colored with temperature, for the conditions corresponding to point *c* of figure 4.6. (Jet: $u_j = 56.6$ *cm/s*, $X_{H_2} = 0.19$; co-flow: $u_c = 4.66$, $X_{O_2} = 1.0$)

Figure 4.22 shows a contour plot of the temperature field $0.5 d$ above the nozzle and a *OH* iso-surface plot for $Y_{OH} = 7.0 \cdot 10^{-4}$ of the seven-cell state. The slightly asymmetric structure was found in most simulations,

but also in the experiments (see, for example, figure 4.4 (e)). In the presented seven-cell structure, one can see, that the largest (upper right) cell has the lowest temperature. This is due to the smaller surface towards the limiting reactant region in the jet, compared to the cell volume.

The iso-surface plot of the OH concentration (figure 4.22 (b)) indicates the shape of the cells, with a strongly burning, partially-premixed region at the flame base and a narrow, diffusion-dominated part higher up. The diffusion dominated part is narrow and closer to the limiting reactant (hydrogen) region.

In addition to the change in jet velocity, simulations for different hydrogen mole fractions were performed. The simulation with $X_{H_2} = 0.18$ (figure 4.6, point D) was performed starting from the five-cell state, obtained at the conditions corresponding to point b , as initial condition. In agreement with the experimental observations, a five-cell flame was obtained. Figure

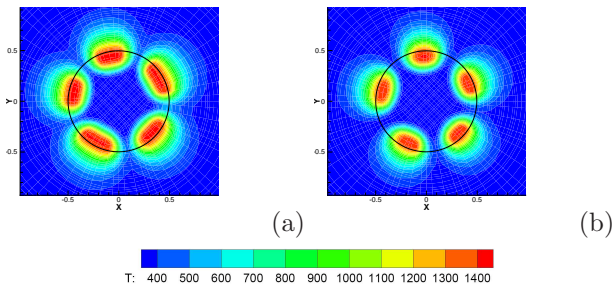


Figure 4.23: Iso temperature plots of the 5-cell flame with a H_2 mole fraction of $X_{H_2} = 0.19$ (a) and $X_{H_2} = 0.18$ (b) on a plane $0.5 d$ above the nozzle. (Jet: $u_j = 37.7 \text{ cm/s}$; co-flow: $u_c = 4.66$, $X_{O_2} = 1.0$)

4.23 shows the two flames with hydrogen mole fractions in the jet of $X_{H_2} = 0.19$ (figure 4.23 (a)) and $X_{H_2} = 0.18$ (figure 4.23 (b)), having maximum temperatures of $1475K$ and $1465K$, respectively. The main difference is the cell size, which is much smaller for the flame with lower hydrogen concentration. The reduction of the fuel concentration results in lower overall reaction intensity, but the reaction intensity in the center of the cells remained almost unchanged. Accordingly, the sizes of the cells are reduced. A similar effect could be seen for the formation of the cells starting from a contiguous flame (see figure 4.12). The reduction of the fuel concentration resulted in a smaller reaction volume, but not in a strongly reduced maximum reaction intensity. This is due to the fast diffusing fuel,

which diffuses into the reaction zone and compensates locally the overall reduced fuel concentration. The less hydrogen is available, the smaller is the volume of strong reaction and therefore the cellular flames.

4.3.3 Variation of the jet velocity profile

Lo Jacono [38, 39] reported on the sensitivity of the resulting cellular mode to the jet inlet velocity profile. This sensitivity, together with the uncertainties associated with the inlet profiles, motivated an additional investigation, where the influence of the steepness of the initial jet velocity profile on the cellular mode was investigated. Figure 4.7 shows the correlation of the normalized wave length of the cellular mode with the square root of the normalized vorticity thickness. Where b and γ are a burner-specific factor and an empirically defined value (0.22 here), respectively.

In the simulations, the vorticity thickness of the jet velocity profile can be varied independently of jet and co-flow velocities. In order to reproduce the experimental observations, different inlet profiles with equal Reynolds number were used. The conditions were those of point B in figure 4.6, where already an eight- and a five-cell state could be stabilized using different inlet profiles (see section 4.3.2).

The velocity profiles were defined by equation (4.4). The cases considered and the cellular structures obtained in the simulations are summarized in the table 4.1. The corresponding inflow profiles are plotted in figure 4.24.

Table 4.1: Considered inlet profiles and resulting cellular structures.

Profile	β	δ	number of cells
P1	0.000	0.050	8
P2	0.042	0.075	7
P3	0.084	0.099	5
P4	0.100	0.150	3

Profiles one and three were applied in the simulations of the eight- and five-cell modes described before. Profile P2 resulted in a seven-cell flame while with P4 a rotating three-cell flame was obtained.

The three-cell mode is rotating. A rotating mode was not observed in the experimental investigations for the given parameters, but in study A (figure 4.3), it was observed that modes with three or less cells were

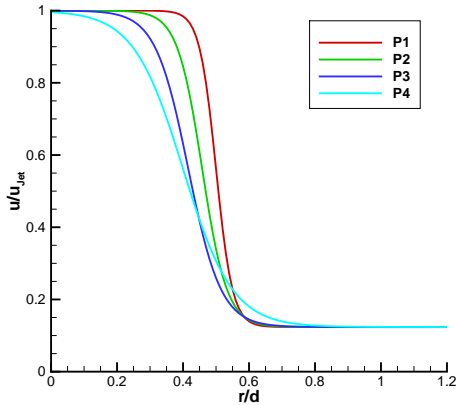


Figure 4.24: Normalized jet inlet velocity profiles with the parameters of table 4.1, leading to a 8, 7, 5 or 3 cell state.

always rotating. The temperature plots $0.5 d$ above the nozzle of the cellular flames obtained with the four different inlet profiles are presented in figure 4.25 with the black circle indicating the size of the nozzle. The location of the flame is closer to the jet axis for the smoother profiles, obtained by increasing β .

The simulations support the experimental finding that the number of cells in the flame is proportional to the square root of the vorticity thickness of the jet inlet velocity independent of the maximum velocity of the jet. Consequently, the cellular mode of the flame depends on the vorticity thickness and not on the jet velocity per se. Figure 4.26 relates the cell size to the vorticity thickness as was done in the analysis of [38]. The correlation shows a very good agreement for the three stationary cellular modes. The rotating three-cell mode does not fit into the plot (blue \diamond), which is due to the definition of the cell size according to equation 4.3. The non uniform cell size requires individual evaluation of the dimension of each cell. If the cell size (λ) is set equal to the measured size of the “stationary” cell (see below), also the three-cell mode follows the relation of figure 4.26 (red \diamond).

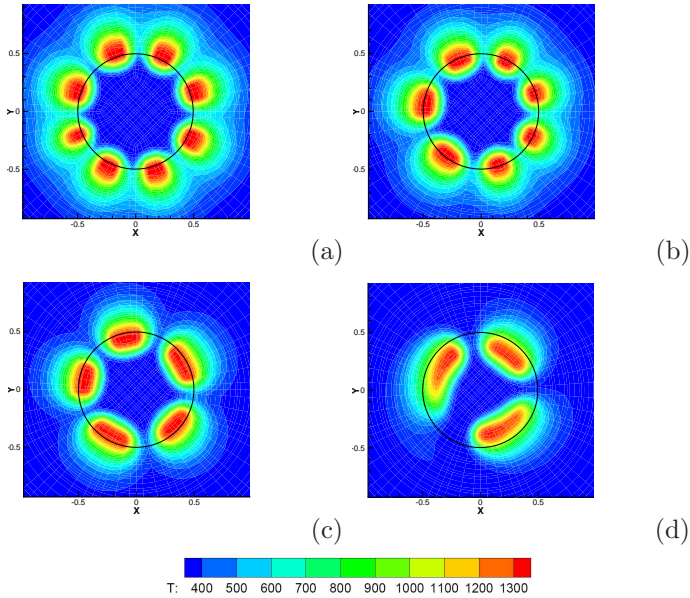


Figure 4.25: Temperature iso-contours on a plane $0.5 d$ above the nozzle for the inlet velocity profiles P1-P4 for figure (a) to (c). (Jet: $u_j = 37.7$ cm/s, $X_{H_2} = 0.19$; co-flow: $u_c = 4.66$, $X_{O_2} = 1.0$)

4.3.4 Rotating cellular flame

Temperature iso-contours on a plane $0.5 d$ above the nozzle for the rotating three-cell mode at different times are shown in figure 4.27. It can clearly be seen, that the rotation is not continuous, but the cells are propagating one by one.

The cells are alternately almost stationary or propagating. During propagation the cells are propagating in clockwise direction for about 100° on the circle formed by the cells. The propagating cells have a zone of high reactivity in front and a weakly burning part behind. After moving close to the next cell, the cell stops and a stationary cell with evenly distributed reaction intensity is formed. The stationary state is retained for almost 40 ms (figure 4.27 (b)-(e), upper left cell) and then starts propagating again. Generally, there are always two almost stationary cells filling out about half of the circle, while on the other half the third cell is propagating with

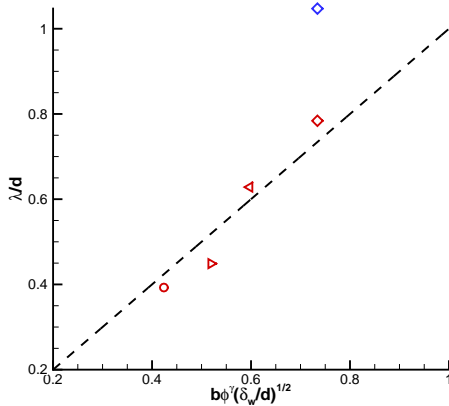


Figure 4.26: Cellular wavelengths of the $X_{H_2} = 0.19$ flame compared to the vorticity thickness equivalent to the comparison of [38] with empirical fitted values of $\gamma = 0.22$ and $b = 2.83$. The symbols are (\circ) for the 8-cell, (\triangleright) for the 7-cell, (\triangleleft) for the 5-cell and (\diamond) for the 3-cell mode (blue for the calculated ($\lambda = \pi d/N_{cell}$) wave number and red for the measured cell size).

a speed of about 0.2 m/s .

Figure 4.28 (a) shows the time history of the temperature (red) at a point located in the flame ($0.191 d, 0.462 d, 0.5 d$). The Fourier transform (blue) shows a maximum at a frequency of 13.02 s^{-1} which corresponds to the interval between the second and the third maximum of the temperature. The second peak at 21.57 s^{-1} corresponds to the minor fluctuations on the high temperature peaks. The computed time frame is not enough to investigate the periodicity in detail, but it gives an idea of the quasi periodicity of the cell rotation.

Figure 4.28 (b) shows the time history of temperature, velocity and species concentrations at the same point ($0.191 d, 0.462 d, 0.5 d$). The point is closer to the oxidizer side of the flame, which results in a relatively large oxygen concentration throughout the simulated interval. The oxygen and hydrogen concentrations increase between the cells, therefore a partially premixed mixture is formed prior to combustion in the propagating cellular flame. The behavior of the axial velocity and temperature are sim-

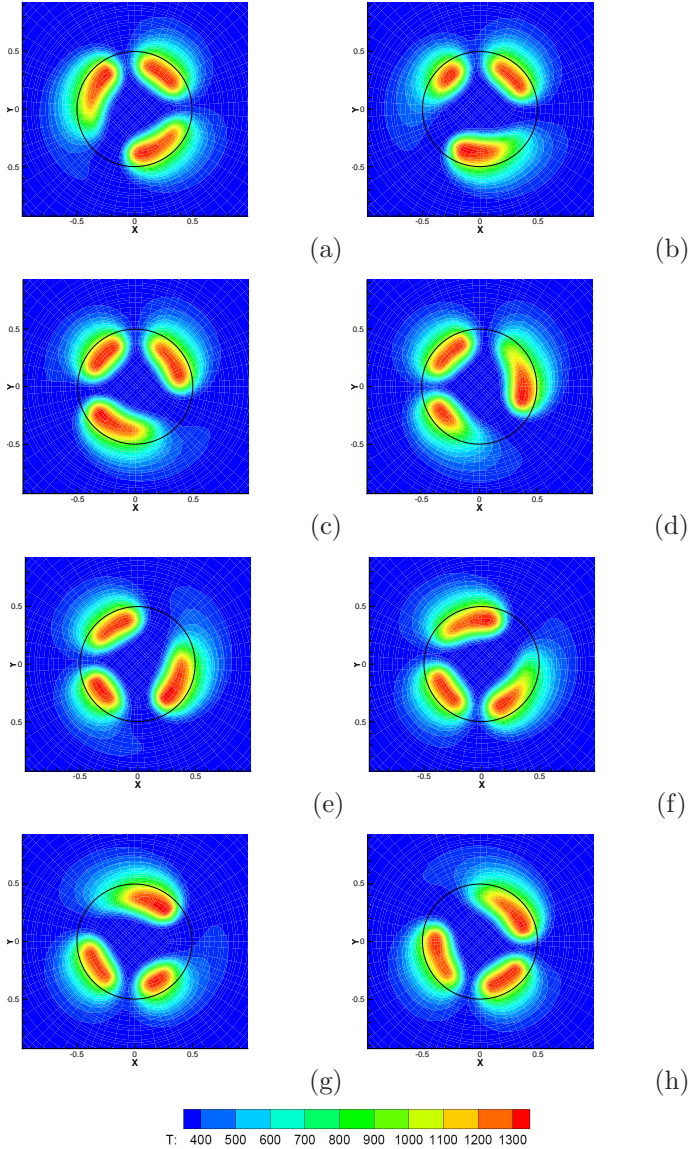


Figure 4.27: Temperature iso-contours on a plane $0.5 d$ above the nozzle for the 3-cell flame with the inlet velocity profile P4. The time interval between two plots is $10ms$. (Jet: $u_j = 37.7 \text{ cm/s}$, $X_{H_2} = 0.19$; co-flow: $u_c = 4.66$, $X_{O_2} = 1.0$)

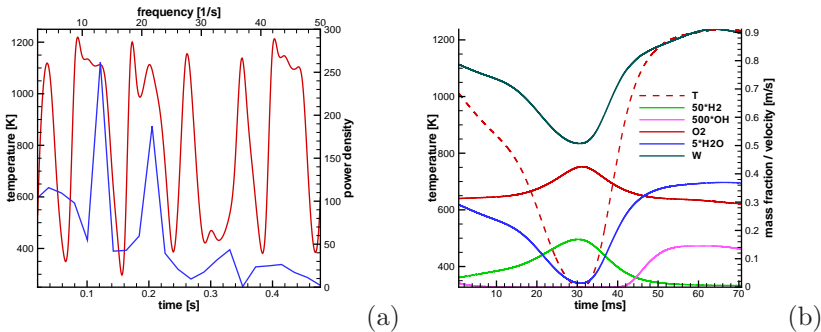


Figure 4.28: (a) Time history of temperature (red line) together with the associated frequency spectra (blue line). (b) Time history of temperature, velocity and species concentration in the point $x = 0.191 d$, $y = 0.462 d$, $z = 0.5 d$ for the rotating 3-cell flame obtained with inlet velocity profile P4. (Jet: $u_j = 37.7 \text{ cm/s}$, $X_{H_2} = 0.19$; co-flow: $u_c = 4.66$, $X_{O_2} = 1.0$)

ilar with a defined minimum and a following sudden increase at 32 ms , when the flame reaches the point of observation. The water concentration increases at the same time, but reaches an almost constant value very quickly together with the decrease of the hydrogen concentration towards zero. The OH concentration, increases 9 ms later and reaches also an almost constant concentration. The further increase of the temperature after the reduction of the fuel concentration to zero, is due to diffusion controlled combustion and the reduced heat conduction in the center of the cellular flame.

The balance of the diffusion, convection and chemical source terms along a circle through the flames ($r = 0.423 d$) is shown in figure 4.29. At the chosen time, an accelerating, a decelerating and a stationary cellular flame are coexisting. The starting point is set to be between the accelerating and the stationary flame. Since the azimuthal angle is increased, the positive x-axis direction is counter-clockwise in the flame and the flames propagate in the negative x-direction. The direction of the flame propagation can be seen in the temperature distribution, where the higher temperature is close to the propagation front. This is very pronounced for the accelerating cell, which is the one on the right side. The three terms (diffusion, convection and reaction) do not completely balance each other, since the flame is not in a steady state. The terms of the energy equation (figure

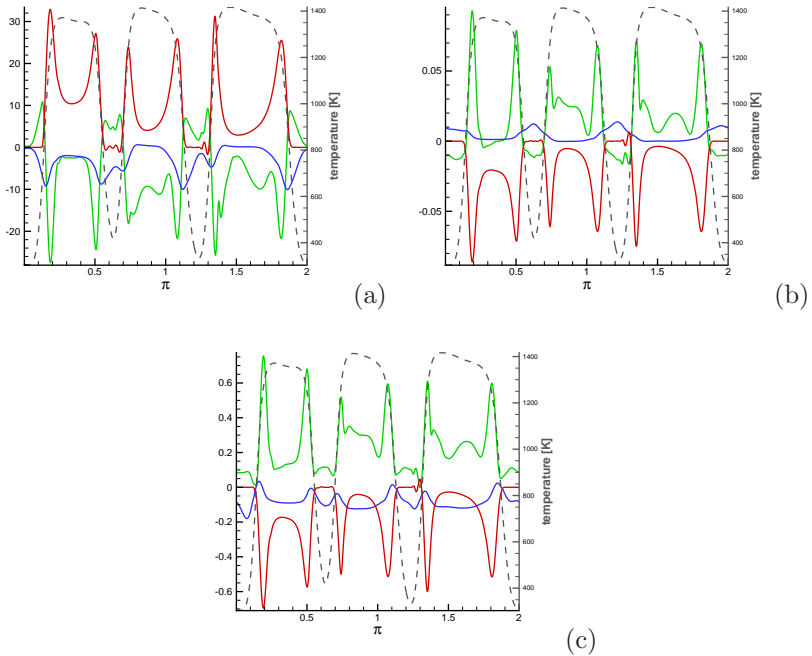


Figure 4.29: The balance of terms in azimuthal direction at $z = 0.5d$ in radial direction ($r = 0.423d$) through a cellular flame. Plotted are the normalized values of (green) the diffusion, (blue) the convection and (red) the reaction term of (a) the energy equation, (b) the hydrogen and (c) oxygen species equations. The temperature distribution (grey) is plotted for determination of the flame location. (Jet: $u_j = 37.7$ cm/s, $X_{H_2} = 0.19$; co-flow: $u_c = 4.66$, $X_{O_2} = 1.0$)

4.29(a)) show the major source of heat on the boundaries of the cellular flames. Heat diffuses partially into the non burning gaps between the flames, but mainly in the radial direction. The convection term reduces the temperature at the peaks of chemical reaction and between the cells, where cold gases propagate in the axial direction. In the middle of the cell, convection plays no role, since the surrounding gasses have similar temperature. As described above, the convection term is important in the axial direction, due to the dominant velocity component, while the diffusion term is dominated by the radial component, due to the high gra-

dients.

The terms of the hydrogen equation show the same peak on the cell boundary, where intense diffusion of fuel balance the chemical term, where the fuel is consumed. The convection term has a minor effect here; it only balances the azimuthal diffused fuel in the non-burning part by convecting new hydrogen from below. The oxygen equation terms (figure 4.29(c)) show similar behavior as the hydrogen equation terms. But the excess of oxygen leads to a negative convection term in the flame zone, because not all the oxygen can be consumed by combustion.

4.4 Conclusions

The direct numerical simulation code, which was described in chapter 2 was used to simulate cellular diffusion jet flames at conditions suggested by the experimental parametric studies performed by Lo Jacono et al. [40, 38]. In These studies diffusion flames close to extinction were investigated with a round, CO_2 diluted hydrogen jet with a co-flowing oxidizer stream.

The experimental set-up of study *A* (figure 4.3), where different cellular modes for different co-flow and jet compositions were reported, was used for the first simulation. For the applied gas compositions a five-cell flame was obtained, which is in agreement with the experiment. This five-cell mode is dominant for the chosen parameters and starting from it, no other cellular mode could be obtained with the available means in simulations. The simulations results for the set-up of the parametric study *B*, where the jet velocity and composition was varied, agreed very well with the experimental findings concerning both, the resulting cellular mode and the observed trends for variations of the jet velocity and the fuel concentration. Unlike the experimental measurements, where only very basic data was available, the simulations provided detailed and well resolved information on the internal cellular structure and the combustion processes. The analysis of the detailed results revealed the triggering preferential diffusion of the reactants in the convex structures of the cellular flames. Further, the partially premixing in the cellular flames was investigated applying the flame index (FI) as an indication of the local flame character. The analysis of the balanced diffusion, convection and chemical terms in different locations in the flame visualized the relevant physical mechanisms in the cellular structure.

In a third study, the dependency of the cellular mode on the initial vorticity thickness of the jet reported in was reproduced numerically. The

predicted correlation of the cellular mode with the initial vorticity thickness was successfully reproduced. Four different initial jet profiles were applied resulting in flames with eight, seven, five and three cellular structures. The three-cell mode, obtained with the jet profile with the largest initial vorticity thickness, was rotating. Inflow profiles with similar vorticity thickness were not investigated experimentally in [39], but earlier investigations [22, 40] showed this rotating behavior in different configurations for cellular modes with three and less flames. The nature of the rotating cellular flame was analyzed in time, where again partial premixing could be shown to be the driving force behind the rotation of the cellular flame.

The comparison of the simulation results with the available experimental results showed good agreement and the detailed numerical data gave detailed insight on the structure of the flames. The analysis of the triggering parameters for the formation of cellular structures in the applied diffusion flame configuration is hindered by the number of involved mechanisms. And the investigation of the pure thermo-chemical instability is complex due to its coupling with the flow field.

Chapter 5

Conclusions and Outlook

5.1 Thesis summary

The subject of the present work is the direct numerical simulation of cellular structures which develop in jet diffusion flames close to extinction. The nature of diffusion flames and diffusion flame instabilities is addressed at the beginning of this thesis.

The first part of this work consisted of the development of the here applied three dimensional, parallel code for reactive flows. The code development was based on an existing spectral element code. The implementation of the detailed evaluation of the chemical source terms and the detailed transport properties were achieved within the scope of this work. These modifications required the change of the temporal integration scheme to a fully implicit one. The resulting code and the conservation equations in their applied form are presented in chapter 2. The code was successfully validated against recent numerical opposed-jet flame results and it showed very good scalability.

In the scope of this work, the here developed code was applied for two different configurations: An opposed-jet flame experimentally investigated by Ciani [10] and a jet diffusion flame configuration based in the experimental work of Lo Jacono [40, 38, 39].

The numerical analysis of the experimentally well documented opposed-jet configuration could reproduce most of the experimental findings. A quantitative comparison of the stationary simulation results with the detailed experimental data was performed showing good agreement within the accuracy of the experimental techniques. Starting from a ring-shaped

edge flame, transient simulations with decreasing oxidizer stream velocity were performed. Dependent on the fuel jet velocity, the edge flame showed either restoration of the diffusion flame or extinction. A critical fuel jet velocity (u_c) could be defined. The analysis of the extinguishing flame could relate this behavior to the velocity field in the burner.

In chapter 4, the experimental set-up, which guided the here presented simulations, and the experimental results of Lo Jacono are summarized. The experimental work consists of two parametric studies with a diluted hydrogen jet and a diluted/pure oxygen co-flow. In the two parametric studies, different parameters were varied: (A) - Variation of jet and co-flow composition. (B) - Variation of jet composition and velocity. Results of both studies could be reproduced numerically with good agreement of the few experimental available data. The simulations of these cellular flames were very time consuming and since they are weakly burning, extinction of the flame was often resulting from a change in the boundary condition. Therefore only few configurations could be reproduced, but the detailed well resolved data gave insight into the internal structure and the chemical reactions within the cellular flames. The resulting picture was the one of a strongly diluted partially premixed flame, which is characterized by very intense reaction at the convex edges of the cellular flames. The convex structure of these edges enables combustion in the considered diluted environment due to thermo-diffusive effects.

The dependence of the cellular mode on the initial jet velocity profile was investigated motivated by [39]. The experimental dependency could be reproduced by variation of the initial inlet velocity profile for a fixed maximum inlet velocity. Four different cellular modes with eight, seven, five and three cells, were obtained and the number of cellular structures showed to be proportional to the steepness of the jet velocity profile. The three-cell mode, which was obtained for the smoothest applied inlet velocity profile, was rotating. Rotating cellular flames were observed experimentally for other configurations in flames with three or less cellular structures [22, 40]

The numerical code which was partially developed in this work, shows very good scalability and can be used to probe the complex interaction between the different physical processes present in combustion and enhance our understanding. The code is applied in several ongoing projects at ETH Zurich.

5.2 Future work

The constant increase of computational capacities provides the possibility to perform more and longer transient simulations of the formation and transition of cellular structures in diffusion flames. The following investigations could lead to interesting findings:

- The simulation of extinction, formation, splitting and combination of cellular structures resulting from a change in boundary conditions could provide valuable information on the influence of flow and stream parameters on the stable cellular structures.
- It was found, that the variation of the inlet profile can change the cellular mode reliable and fast. This could be used to generate optimized initial fields for the simulation with higher jet velocities in order to map the experimental investigated range.
- The analysis of the presented rotating cellular modes together with further simulations might increase the understanding of the interaction of premixed and diffusion guided combustion.
- Detailed comparison of the rotating and stationary modes could reveal the driving mechanism of the rotation. The onset limit of rotation should be analyzed for different burner geometries and sizes in order to decouple the flame dimensions from the burner geometry (can a four cell-mode be rotating in burner with larger nozzle diameter?).
- A comparison of the rotating and the flickering flame (observed for high Lewis numbers) concerning the flame structure, the involved frequencies and the Lewis number range of their occurrence could provide interesting information.

Bibliography

- [1] C. Appel, J. Mantzaras, R. Schaeren, R. Bombach, and A. Inauen. Turbulent catalytically stabilized combustion of hydrogen/air mixtures in entry channel flows. *Combust. Flame*, 140(1-2):70–92, 2005. Article 0010-2180.
- [2] P. N. Brown, G. D. Byrne, and A. C. Hindmarsh. Vode - a variable-coefficient ode solver. *SIAM J. Sci. Stat. Comp.*, 10(5):1038–1051, 1989. Article 0196-5204.
- [3] J. Buckmaster. Edge-flames. *Progr. Energy Comb. Sci.*, 28(5):435–475, 2002. Review 0360-1285.
- [4] S. P. Burke and T. E. W. Schumann. Diffusion flames. *Ind. Eng. Chem.*, 20(1):998–1004, 1928. Article 0019-7866.
- [5] V. V. Bychkov and M. A. Liberman. Dynamics and stability of pre-mixed flames. *Physics Reports-Review Section Of Physics Letters*, 325(4-5):116–237, 2000. Review 0370-1573.
- [6] G. D. Byrne and A. C. Hindmarsh. PVODE, an ode solver for parallel computers. *Int. J. High Perf. Comp. Appl.*, 13(4):354–365, 1999.
- [7] S. Cheatham and M. Matalon. A general asymptotic theory of diffusion flames with application to cellular instability. *J. Fluid Mech.*, 414:105–144, 2000.
- [8] R. Chen, G. B. Mitchell, and P. D. Ronney. Diffusive-thermal instability and flame extinction in nonpremixed combustion. *Proc. Comb. Inst.*, 24, pages 213–221, 1992.
- [9] B. T. Chu and L. S. G. Kovaszny. Non-linear interactions in a viscous heat-conducting compressible gas. *J. Fluid Mech.*, 3(5):494–514, 1958. Article 0022-1120.

- [10] A. Ciani. *Hydrogen and Methane Edge and Diffusion Flames in Opposed Jet Configurations: Structure and Stability*. Dissertation, Swiss Federal Institute of Technology Zurich, 2006.
- [11] A. Ciani, W. Kreutner, W. Hubschmid, C. E. Frouzakis, and K. Boulouchos. Experimental investigation of the morphology and stability of diffusion and edge flames in an opposed jet burner. *Combust. Flame*, 150(3):188–200, 2007. Times Cited: 0 0010-2180.
- [12] P. Clavin. Dynamic behavior of premixed flame fronts in laminar and turbulent flows. *Progr. Energy Comb. Sci.*, 11(1):1–59, 1985. Review 0360-1285.
- [13] S. D. Cohen and A. C. Hindmarsh. CVODE, a stiff/nonstiff ode solver in c. Technical report, Center for Computational Sciences & Engineering, 1995.
- [14] E. L. Cussler. *DIFFUSION Mass Transfer in Fluid Systems*. Cambridge University Press, 2nd edition, 1997.
- [15] M. R. Dongworth and A. Melvin. Transition to instability in a steady hydrogen-oxygen diffusion flame. *Comb. Sci. Tech.*, 14(4-6):177–182, 1976. Article 0010-2202.
- [16] V. Favier and L. Vervisch. Edge flames and partially premixed combustion in diffusion flame quenching. *Combust. Flame*, 125(1-2):788–803, 2001. 0010-2180.
- [17] P. F. Fischer. Analysis and application of a parallel spectral element method for the solution of the navier-stokes equations. *Comp. Meth. Appl. Mech. Eng.*, 80(1-3):483–491, 1990. Article 0045-7825.
- [18] C. E. Frouzakis, J. Lee, A. G. Tomboulides, and K. Boulouchos. Two-dimensional direct numerical simulation of opposed-jet hydrogen-air diffusion flame. In *Proc. Comb. Inst.*, 27, pages 571–577, 1998.
- [19] C. E. Frouzakis, A. G. Tomboulides, J. Lee, and K. Boulouchos. From diffusion to premixed flames in an h-2/air opposed-jet burner: The role of edge flames. *Combust. Flame*, 130(3):171–184, 2002.
- [20] C. E. Frouzakis, A. G. Tomboulides, J. Lee, and K. Boulouchos. Transient phenomena during diffusion/edge flame transitions in an opposed-jet hydrogen/air burner. *Proc. Comb. Inst.*, 29:1581–1587, 2003. Part 2.

- [21] C. E. Frouzakis, A. G. Tomboulides, P. Papas, P. F. Fischer, R. M. Rais, P. A. Monkewitz, and K. Boulouchos. Three-dimensional numerical simulations of cellular jet diffusion flames. *Proc. Comb. Inst.*, 30:185–192, 2005. Part 1.
- [22] M. Füri. *Non-Premixed Jet Flame Instabilities*. Dissertation, Ecole Polytechnique Federale de Lausanne, 2001.
- [23] J. E. Garside and B. Jackson. Polyhedral diffusion flames. *Nature*, 168(4286):1085–1085, 1951. Letter 0028-0836.
- [24] J. E. Garside and B. Jackson. The formation and some properties of polyhedral burner flames. *Proc. Comb. Inst.*, 4:545–552, 1953.
- [25] N. Goren-Inbar, N. Alperson, M. E. Kislav, O. Simchoni, Y. Melamed, A. Ben-Nun, and E. Werker. Evidence of hominin control of fire at gesher benot ya’aqov, israel. *Science*, 304(5671):725–727, 2004. Article 0036-8075.
- [26] A. C. Hindmarsh. Lsode, and lsodi, two new initial value ordinary differential equation solvers. *ACM SIGNUM Newsletter*, 15(4):10–11, 1980.
- [27] H. G. Im, J. H. Chen, and J. Y. Chen. Chemical response of methane air diffusion flames to unsteady strain rate. *Combust. Flame*, 118(1-2):204–212, 1999. Article 0010-2180.
- [28] S. Ishizuka and H. Tsuji. Effects of transport-properties and flow non-uniformity on the temperature of counterflow diffusion flames. *Comb. Sci. Tech.*, 37(3-4):171–191, 1984. Article 0010-2202.
- [29] R. J. Kee, G. Dixon-Lewis, J. Warnatz, M.E. Coltrin, and J. A. Miller. A fortran computer code package for the evaluation of gas-phase multicomponent transport properties. 1996.
- [30] R. J. Kee, F. M. Rupley, and J. A. Miller. Chemkin-ii: A fortran chemical kinetics package for the analysis of gas phase chemical kinetics. *SANDIA REPORT*, 1989.
- [31] J. S. Kim. Linear analysis of diffusional-thermal instability in diffusion flames with lewis numbers close to unity. *Combust. Theory Modelling*, 1:13–40, 1997.
- [32] J. S. Kim, F. A. Williams, and P. D. Ronney. Diffusional-thermal instability of diffusion flames. *J. Fluid Mech.*, 327:273–301, 1996.

- [33] J. D. Lambert. *Numerical methods for ordinary differential systems: the initial value problem*. John Wiley & Sons Ltd., 1991.
- [34] J. Lee. *Simulation of Two-dimensional Chemically Reactive Flows*. Dissertation, Princeton University, 1996.
- [35] J. Lee, C. E. Frouzakis, and K. Boulouchos. Two-dimensional direct numerical simulation of opposed-jet hydrogen/air flames: Transition from a diffusion to an edge flame. *Proc. Comb. Inst.*, 28:801–806, 2000. Part 1.
- [36] J. Li, Z. Zhao, A. Kazakov, and F. L. Dryer. An updated comprehensive kinetic model of hydrogen combustion. *Int. J. Chem. Kin.*, 36:566–575, 2004.
- [37] A. Linan. Asymptotic structure of counterflow diffusion flames for large activation-energies. *Acta Astronautica*, 1(7-8):1007–1039, 1974. Article 0094-5765.
- [38] D. Lo Jacono. *Experimental Study of Cellular Instabilities in Non-Premixed Flames*. Dissertation, Ecole Polytechnique Federal de Lausanne, 2005.
- [39] D. Lo Jacono and P. A. Monkewitz. Scaling of cell size in cellular instabilities of non-premixed jet flames. *Combust. Flame*, submitted May, 2007, 2007.
- [40] D. Lo Jacono, P. Papas, and P. A. Monkewitz. Cell formation in non-premixed, axisymmetric jet flames near extinction. *Combust. Theory Modelling*, 7:635–644, 2003.
- [41] M. Matalon. Intrinsic flame instabilities in premixed and non-premixed combustion. *Ann. Rev. Fluid Mech.*, 39:163–191, 2007. Review 0066-4189.
- [42] P. Metzener and M. Matalon. Diffusive-thermal instabilities of diffusion flames: onset of cells and oscillations. *Comb. Theory Mod.*, 10(4):701–725, 2006. Article 1364-7830.
- [43] C. E. Mortimer. *Chemie, Das Basiswissen der Chemie*. Georg Thieme Verlag Stuttgart - New York, 6 edition, 1996.
- [44] P. Papas, R. M. Rais, P. A. Monkewitz, and A. G. Tomboulides. Instabilities of diffusion flames near extinction. *Comb. Theory Mod.*, 7(4):603–633, 2003. Article 1364-7830.

- [45] G. L. Pellett, K. M. Isaac, W. M. Humphreys, L. R. Gartrell, W. L. Roberts, C. L. Dancy, and G. B. Northam. Velocity and thermal structure, and strain-induced extinction. of 14 to 100 *Combust. Flame*, 112(4):575–592, 1998. Article 0010-2180.
- [46] N. Peters. Laminar diffusion flamelet models in non-premixed turbulent combustion. *Progr. Energy Comb. Sci.*, 10(3):319–339, 1984. Review 0360-1285.
- [47] T. Poinso and D. Veynante. *Theoretical and Numerical Combustion*. 2005.
- [48] A. E. Potter and J. N. Butler. A novel combustion measurement based on the extinguishment of diffusion flames. *Ars J.*, 29(1):54–56, 1959. Note 0097-4056.
- [49] R. M. Rais. *Investigations of Diffusion Flame Instabilities*. Dissertation, Ecole Polytechnique Federale de Lausanne, 2003.
- [50] Y. Saad. *Iterative Methods for Sparse Linear Systems*. 2000.
- [51] A. G. Tomboulides. *Direct and Large-Eddy Simulation of Wake Flows: Flow Past a Sphere*. Dissertation, Princeton University, 1993.
- [52] A. G. Tomboulides, J. C. Y. Lee, and S. A. Orszag. Numerical simulation of low mach number reactive flows. *J. Sci. Comp.*, 12(2):139–167, 1997.
- [53] D. C. Wilcox. *Basic Fluid Mechanics*. 1997.
- [54] F. A. Williams. *Combustion Theory*. Comb. Sci. Engineering Series. Perseus Books Publishing, 2nd edition, 1985.
- [55] Y. Yamashita, M. Shimada, and T. Takeno. A numerical study on flame stability at transition point of jet diffusion flames. *Proc. Comb. Inst.*, 26:27–34, 1996. Article 0082-0784 Part 1.
- [56] Y. Zhang, P. D. Rooney, E. V. Roegner, and J. B. Greenberg. Lewis number effects on flame spreading over thin solid fuels. *Combust. Flame*, 90(1):71–83, 1992. Article 0010-2180.

Appendix A

CVODE

CVODE is a stable stiff ODE solver. These ODE solvers include LSODE [26], VODE [2] and VODEPK. While LSODE and VODE are general purpose solvers for stiff and non-stiff systems using direct methods, VODEPK is equipped for the treatment of large stiff systems using Krylov iteration techniques. VODEPK also provides the possibility of user-supplied preconditioning of the matrix for the treatment of the dominant source of stiffness. In 1995 Cohen et al. [13] presented CVODE as a substitution of all former codes. All these ODE solvers solve problems of the form:

$$\frac{d\mathbf{Y}}{dt} = f(\mathbf{Y}) \quad (\text{A.1})$$

CVODE is written in C, but has a Fortran interface and the possibilities were enhanced by three different Krylov methods which are used in conjunction with Newton iteration. In the scope of this work, only the generalized minimal residual method (GMRES) is used (see [50]). Byrne et al. [6] presented a parallel version of CVODE, which was called PVODE, but recently the two codes were combined into one single code which is simply called CVODE.

The Fortran interface of CVODE (FCVODE) is used in order to couple the Fortran three dimensional DNS code to the CVODE which is written in C. The following subroutines have to be called in order to initialize the parallel CVODE for Newton iteration and GMRES technique:

routine	description
FNVINITP	initializes the parallel vector module
FCVMALLOC	sets various problem and solution parameters and allocates internal memory
FCVSPGMR	initializes the scaled preconditioned GMRES solver

The routine FNVINITP is the Fortran interface to the initialization routine of CVOICE. The inputs are the name of the MPI communicator as well as the local and global number of equations of the problem. Since each node has to make this initializing call, the evaluation of the global number of equations requires parallel communication. The routine FCVMALLOC provides required problem and solution specifications, specifies optional inputs and allocates internal memory. The inputs are the initial time and \underline{Y} , the basic integration method, which is chosen to be the backward differentiation formula (BDF) here, the iteration method (Newton) and the absolute and relative tolerances. The input vector \underline{Y} (see equation (A.1)) is arranged in vectorial form and contains the local temperature and species fields in the presented case. The call to the routine FCVSPGMR initializes the scaled preconditioned GMRES solution method for the linear system. Different types of preconditioning are supported by the code. No preconditioning is applied here mainly due to the complicated structure of the matrix due to the three dimensional problem. Other inputs include the Gram-Schmidt process type (modified is applied), the maximum Krylov subspace dimension and the linear convergence tolerance factor.

The call to the CVOICE for the integration of the thermochemistry part is performed as:

```
CALL FCVOICE (tout, t,  $\underline{Y}$ , ITASK, IER)
```

where t_{out} is the time of the desired solution, t is the actual time and \underline{Y} is the above discussed vector which is input and output argument here. The input is \underline{Y} at time t and \underline{Y} at time t_{out} is the resulting field of the integration. ITASK is a task indicator and IER a completion flag. The most important interaction of the user with CVOICE is to provide a subroutine which calculates the right-hand side the ODEs of equation (A.1) from the CVOICE internal temperature and species fields:

```
SUBROUTINE FCVFUN (CVTIME,  $\underline{Y}$ ,  $\dot{\underline{Y}}$ , ..., IER)
```

where CVTIME is the time at which CVOICE evaluates the the right-hand side, \underline{Y} are the CVOICE internal temperature and species

fields and $\dot{\underline{Y}}$ the desired solution of this routine. This routine evaluates the species and energy equations according to the frozen velocity field and the species and temperature fields provided by the iterative solver. It is also in this routine, where parallel communication for the evaluation of the spatial derivations is required.

Appendix B

Curriculum Vitae

1975	Born on May, 25 th , Zurich
1982 - 1990	Elementary and secondary school, Fallanden ZH
1990 - 1995	Grammar school (focus: economy), Zurich
1996 - 1998	Study in economy, University of Zurich
1998 - 2003	Study of mechanical engineering, ETH Zurich
2003	Diploma in mechanical engineering, ETH Zurich
2003 - 2007	Doctoral student and teaching assistant at the Institute of Energy Technology / LAV, ETH Zurich